Characterization of spatiotemporal couplings in ultrashort pulses

Master's Thesis

by Yuhao Zou

Supervisor: Olle Lundh

Examiner: Adam Kinos

LRAP 628
Division of Atomic Physics
Department of Physics, Lund University
June 2026

Abstract

When ultrashort pulses propagate through common optical elements, such as gratings and thick lenses, they inevitably acquire spatiotemporal couplings (STCs), which are nonseparable chromatic aberrations. This phenomenon fundamentally stems from the broad spectral bandwidth inherent to ultrashort pulses. STCs can significantly reduce peak intensity, enlarge the focal spot, and thus limit the optimal performance of ultrashort pulses in their applications such as high-harmonic generation (HHG) and laser-driven particle acceleration. This thesis aims to characterize the STCs in a multi-terawatt optical parametric chirped-pulse amplification (OPCPA) laser system. The primary method employed is the Iterative Multispectral Phase Analysis for LAsers (IMPALA) technique, which combines far-field beamlet cross-correlation with a Gerchberg-Saxton (GS) phase-retrieval algorithm. To achieve this, we developed and optimized stable data-processing programs, including spatial Fourier filtering and complex phase averaging. The technique was first validated using a continuous-wave fiber laser and subsequently applied to the OPCPA system using both a single-shot mask with 12 pinholes and a multi-rotation mask with 10 pinholes. The results reveal that while the system's wavefront is well optimized by a deformable mirror near its central wavelength (850 nm), it exhibits significant chromatic aberrations at the spectral edges (e.g., 830 nm), primarily exhibiting chromatic spatial tilt (pulse-front tilt) and oblique astigmatism. Furthermore, the quantitative accuracy of the IMPALA algorithm was verified by introducing a defined amount of aberrations, such as astigmatism, x-coma, and spherical aberration via the deformable mirror, demonstrating agreement with theoretical predictions.

Public Science Summary

Ultrashort laser pulses are like a camera flash that blinks in a mere fraction of a trillionth of a second. Achieving such a short duration requires the laser to simultaneously contain a wide blend of different colors, also known as a broad spectrum. These ultrashort and energetic pulses can be useful scientific tools in lots of areas. They can capture the fastest processes in nature, such as the movement of electrons within atoms, and generate enormous bursts of peak power necessary for driving advanced technologies like compact particle accelerators and high-harmonic generation.

However, this multi-colored nature introduces a significant physical challenge. When this broad spectrum of light travels through standard optical components, such as glass lenses or gratings, the different colors bend and propagate at slightly different speeds and angles. As a result, the colors lose their perfect alignment, smearing out in both space and time. This complex distortion is known as a spatiotemporal coupling (STC). Simply put, STCs prevent the laser from focusing perfectly into a single, intensely tight spot, which dramatically reduces the maximum power the laser can deliver. Before these distortions can be corrected, they must be accurately mapped and measured. This thesis focuses on diagnosing STCs in a massive, multi-terawatt high-power laser system. To achieve this, a novel diagnostic technique called IMPALA (Iterative Multispectral Phase Analysis for LAsers) was used. The method works by placing a special mask with a pattern of tiny pinholes directly into the laser beam before focusing optics. This mask splits the large beam into several smaller beamlets. A camera then captures the complex interference patterns created when these smaller beamlets overlap at the focal point. Using customized computer algorithms, these recorded patterns are decoded to reconstruct the distortion maps for individual wavelengths inside the laser pulse. By applying this technique, the research characterized aberrations within the high-power laser. The results showed that while the high-power laser was focused by a deformable mirror, the colors at the outer edges of the spectrum were clearly tilted and distorted. Characterizing these hidden STCs is an important first step toward correcting them, paving the way for building sharper and more powerful lasers for next-generation scientific breakthroughs.

Acknowledgements

First of all, I would like to thank my supervisor Olle Lundh, who has always been willing to discuss the project with me in person and share his knowledge. I feel fortunate to join your research group and have learned a lot in this interesting area. I also want to thank all the group members in the Ultra-high intensity laser group. I would like to extend my thanks to Andrea and Flanish for their help with my experiment, and for sharing their nice lunch place GB nation. Thanks to Erik and Carola for being so friendly and sharing their ideas in physics with me.

I also want to thank all my classmates in Photonics and my friends in Lund for making these two years so memorable, especially Lixuan, Shijun, Samuele and Houda. Lixuan, thank you for organizing so many interesting activities and sharing your taste in music. Shijun, thanks for the countless discussions on physics and photography, for the delicious dinners, and for your help with my film development. Also good to have friends like both of you that almost never reject my fika invitations. Samuele, thanks for sharing a lot of Italian cultures and foods. Houda, thanks for the discussions regarding my thesis, from which I benefit a lot.

I would like to sincerely thank my family, especially my parents, for their unwavering support of my decisions.

Finally, I want to thank my girlfriend, Shuwei. I feel fortunate to have you by my side. Thank you for your constant love and support.

List of abbreviations

STC - Spatiotemporal coupling
PFT - Pulse-front tilt
PFC - Pulse-front curvature
IMPALA - Iterative Multispectral Phase Analysis for LAsers
OPCPA - Optical parametric chirped-pulse amplification
HHG - High-harmonic generation
DM - Deformable mirror
CPA - Chirped Pulse Amplification
CW - Continuous wave
FWHM - Full-width at half-maximum
CEP - Carrier-envelope phase
GD - Group delay
GDD - Group delay dispersion
MSE - Mean square error
FFT - Fast Fourier Transform
BBO - Beta-barium borate
DFG - Difference-frequency generation
ND - Neutral density
GS - Gerchberg-Saxton
SPP - Spatial phase perturbation
DPR - Double-phase retrieval
MPR - Multiple-phase retrieval
HIO - Hybrid Input-Output
PV - Peak-to-Valley
RMS - Root-mean-square

Contents

1 Introduction

Since the conception in 1960s, laser technology has been continuously developing. Historically, the primary approach to increasing laser peak power and intensity has been to shorten the pulse duration. The development of Q-switching and mode-locking techniques, made the generation of ultrashort laser pulses (picosecond and eventually femtosecond regimes) with peak powers in the MW and GW range possible. However, amplifying these ultrashort pulses with high peak intensities would easily damage the optical components of the amplifier, which limited further progress toward shorter and more intense pulses of shorter and stronger pulses. This limitation was overcome with the invention of chirped pulse amplification (CPA) [1]. The CPA technique has pushed the current laser systems with compact structures to have higher peak power in the TW and PW range and shorter duration in short femtosecond domain.

Ultrashort laser pulses, especially those generated by chirped pulse amplification (CPA) technology, are broadband and often limited by chromatic dispersion and optical aberrations when propagating through typical CPA system components, such as expanders, compressors, and dispersive lenses. These optical elements can cause different frequency components of the electromagnetic field to focus differently in space. This phenomenon, where the electric field cannot be mathematically separated into independent spatial and temporal components, is known as spatiotemporal couplings (STCs). STCs can affect the performance of ultrashort pulses in their applications. Apart from simply reducing the peak intensity, STCs disrupt the precise symmetry and timing of the electromagnetic field at the focus [2]. In non-linear applications like high-harmonic generation and attosecond science, this misalignment ruins the stringent phase-matching conditions required for clean emission [3], while in the laser wakefield acceleration, STCs can steer the pointing of the electrons [4].

The most common fundamental STCs in ultrashort laser systems include pulse-front tilt (PFT), typically induced by tilted gratings or prisms, and pulse-front curvature (PFC), which often arises from the chromatic aberrations of lenses. Various spatially resolved measurement techniques have been developed to characterize these STCs. The spatially-resolved measurement techniques, such as SPIDER [5], are extended to one or more spatial dimensions to resolve STCs. RED-SEA-TADPOLE [6] is based on the spectral interference of an unknown pulse with a known reference pulse to characterize STCs. TERMITES [7], and INSIGHT [8] are based on self-referenced Fourier-transform spectroscopy (FTS), using a spatially filtered beam as the reference for the interference. While these methods can provide comprehensive spatiotemporal profiles, they generally rely on complex and expensive optical setups, require hard-to-obtain reference beams, or demand the scanning of hundreds of images. Consequently, they are difficult to implement as routine, in-situ diagnostic tools in low-repetition rate, high-power laser systems.

The aim of this thesis is to utilize a novel technique named IMPALA (Iterative Multispectral Phase Analysis for LAsers) [9],which is based on a far-field beamlet cross-correlation technique [10] to characterize STCs. IMPALA offers a minimally intrusive approach by simply placing a mask with specially arranged pinholes before the focusing optics. The spectrally resolved wavefront can then be reconstructed from far-field speckle patterns by using only a few laser shots, or even a single shot.

At the Lund Laser Centre (LLC), a multi-terawatt laser system, based on optical parametric chirped pulse amplification (OPCPA), is capable of delivering ultrashort pulses with a pulse duration of 9 fs (FWHM), pulse energies of up to 250 mJ, and a central wavelength of approximately 850 nm at a 10 Hz repetition rate. Although this system has been highly optimized for maximum energy delivery, the detailed spatiotemporal properties of its output beam have not yet been fully characterized. Given that the IMPALA technique requires minimal intrusion into the existing optical setup, uses a simple mask structure, and extracts wavefront information from very few images, implementing IMPALA at the LLC represents a promising approach to comprehensively diagnose and map previously unknown spatiotemporal couplings.

1.1 Thesis outline

This thesis is structured as follows: Chapter 2 provides the theoretical background, introducing the mathematical representation of ultrashort pulses, Fourier optics, primary optical aberrations, and the physical origins of spatiotemporal couplings (STCs) such as pulse-front tilt and curvature. Chapter 3 discusses the principles of the Gerchberg-Saxton (GS) algorithm, its convergence properties, and its modern variants for phase retrieval. Chapter 4 introduces the experimental setups and methodology. It describes the fiber laser and the multi-terawatt OPCPA system, the physical design and resolution limits of the IMPALA masks, and the complete computational pipeline for data processing. Chapter 5 presents the results and discussion. It analyzes the phase retrieval from the fiber laser, evaluates the single-shot and multi-rotation IMPALA measurements on the OPCPA system, and validates the algorithm's quantitative accuracy using astigmatism and primary spherical aberration introduced by the deformable mirror (DM). Chapter 6 summarizes the main conclusions of this work and outlines potential future improvements.

2 Theory

2.1 Ultrafast optics

Compared to continuous-wave lasers that can be fully described by their spatial field distributions, ultrashort laser pulses require a rigorously coupled treatment of their spatial, temporal, and spectral characteristics. In the femtosecond regime, the physical length of a pulse is reduced to a micrometer scale. This localized wave packet makes its temporal envelope highly sensitive to the dispersive properties of optical materials and the geometry of optical components [11].

2.1.1 Representation of ultrashort pulses

Mathematically, a monochromatic wave in time and space can be written as

$$U(\mathbf{r}, t) = U(\mathbf{r}) \exp(j\omega t), \tag{2.1}$$

where $U(\mathbf{r})$ is the complex amplitude and $\omega = 2\pi\nu$ is the angular frequency. Now, considering only the time domain, an ultrashort optical pulse of central frequency ν_0 can be represented by an oscillating carrier wave modulated by a slowly varying complex envelope as shown in Figure 2.1:

$$U(t) = A(t) \exp[j(\omega_0 t + \phi(t))] \tag{2.2}$$

where ω_0 is the central angular frequency and $A(t)$ is the complex envelope which can be characterized by magnitude $|A(t)|$ and phase $arg\{A(t)\} = \phi(t)$, such that the intensity $I(t) = |U(t)|^2 = |A(t)|^2$ [11]. The real electric field $U(t)$ at a fixed spatial position is commonly expressed analytically as the real part of a complex field:

$$Re\{U(t)\} = |A(t)| \cos[\omega_0 t + \phi(t)] \tag{2.3}$$

Taking the Fourier transform, the pulse can be described in the spectral domain as:

$$V(\nu) = \mathcal{F}\{U(t)\} = |V(\nu)| \exp[j\psi(\nu)] \tag{2.4}$$

where $\psi(\nu)$ is the spectral phase and the spectral intensity is $S(\nu) = |V(\nu)|^2$. For analytical simplicity, the intensity profile of ultrashort pulses is frequently modeled using a Gaussian function. The temporal envelope of an unchirped (also called transform-limited) Gaussian pulse is given by:

$$A(t) = A_0 \exp\left(-\frac{t^2}{2\tau_{1/e}^2}\right) \tag{2.5}$$

where $\tau_{1/e}$ is the half-width at $1/e$ maximum of the intensity. The full-width at half-maximum (FWHM) of the intensity profile, commonly referred to as the pulse duration τ_{FWHM}, relates to this parameter via $\tau_{FWHM} = \tau_{1/e}\sqrt{2\ln 2}$.

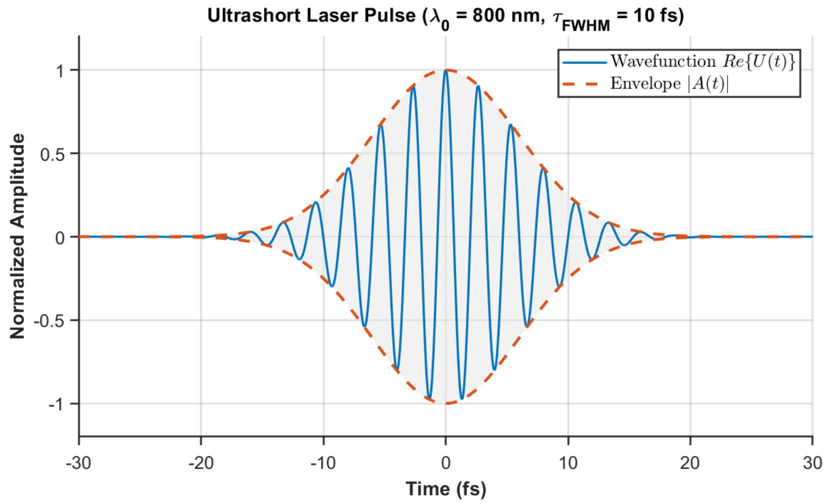

Figure 2.1: Temporal representation of an simulated ultrashort pulse of 10 fs, and $\phi(t) = 0$, showing the rapidly oscillating carrier wavefunction $Re\{U(t)\}$ constrained by an envelope $|A(t)|$.

Because the temporal duration and the spectral bandwidth of the pulse are fundamentally linked through a Fourier transform, it is mathematically impossible to shorten a pulse arbitrarily without correspondingly broadening its spectrum. For a transform-limited Gaussian pulse, the duration at full-width of half maximum τ_{FWHM} and the spectral width $\Delta\nu$ are constrained by the time-bandwidth product:

$$\tau_{FWHM}\Delta\nu = 0.44 \tag{2.6}$$

A pulse that satisfies this fundamental equality is transform-limited, representing the absolute shortest duration achievable for a specific spectral width.

2.1.2 Chromatic dispersion and spectral phase

When a broadband ultrashort pulse propagates through a dielectric medium, it inevitably experiences chromatic dispersion. Because the refractive index $n(\omega)$ of optical materials varies with frequency, different spectral components accumulate different phase shifts. To analyze this temporal distortion, it is convenient to switch to the frequency domain and expand the spectral phase $\psi(\omega)$ in a Taylor series around the central frequency ω_0:

$$\psi(\omega) \approx \psi_0 + \frac{\partial\psi}{\partial\omega}(\omega-\omega_0) + \frac{1}{2}\frac{\partial^2\psi}{\partial\omega^2}(\omega-\omega_0)^2 + \frac{1}{6}\frac{\partial^3\psi}{\partial\omega^3}(\omega-\omega_0)^3 + \ldots \tag{2.7}$$

The first term ψ_0 represents the absolute phase, related to the carrier-envelope phase (CEP). The second term is the group delay (GD), which dictates the arrival time of the pulse envelope. The third term $\partial^2\psi/\partial\omega^2$ is first order derivative of the GD, thus defined as the group delay dispersion (GDD), which also corresponds to chirp.

2.1.3 Chirped pulse

In multi-terawatt systems relying on chirped pulse amplification (CPA), managing this dispersion is crucial. In general, the CPA technique is to broaden an ultrashort pulse, then amplify the pulse at an intensity below the damage threshold of the amplifier and finally compress the pulse to a femtosecond or picosecond pulse duration. The stretching and compressing processes are achieved by the introduction of a frequency dependent delay in the pulse spectrum.

The second time derivative of $\ddot{\phi} = \partial^2\phi/\partial t^2$ shows how the instantaneous frequency, $\omega_i = \omega_0 + \dot{\phi}$, of the pulse varies with respect to time. The chirp parameter is defined as

$$a = \frac{1}{2}\ddot{\phi}\tau \tag{2.8}$$

If $a < 0$, the instantaneous frequency is decreasing, and the pulse is down-chirped [as shown in Figure 2.2 (b)]. If $a > 0$, the instantaneous frequency is increasing, and then the pulse is up-chirped [(as shown in Figure 2.2 (c)]. For a Gaussian pulse with a complex envelop $A(t) = A_0 \exp(-t^2/\tau) \exp(jat^2/\tau)$ [11], the time derivative $\dot{\phi}$ is a linear function, so that the pulse is linearly chirped.

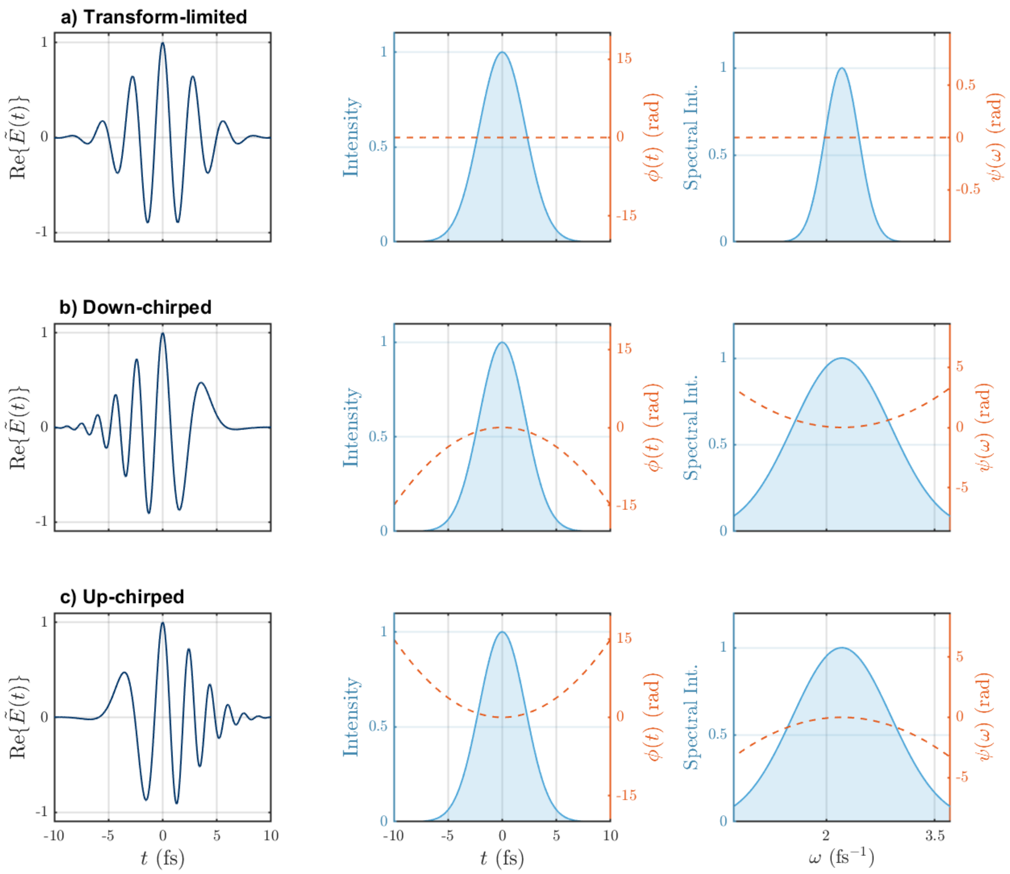

Figure 2.2: Temporal and spectral profiles of different chirped Gaussian pulses with FWHM width 5 fs and central angular frequency 2.216 fs^{-1} corresponding to central wavelength 900 nm. (a) Transform-limited pulse; (b) Down-chirped pulse of chirp parameter $a = -3$; (c) Up-chirped pulse of chirp parameter $a = 3$

2.2 Fourier optics basics

Mathematically, an arbitrary function $f(t)$ can be analyzed as a superposition of harmonic functions of different frequencies with different complex amplitudes:

$$f(t) = \int_{-\infty}^{\infty} F(\nu) \exp(j2\pi\nu t) d\nu \tag{2.9}$$

where ν is the frequency, and the complex amplitude $F(\nu)$ is the Fourier transform of $f(t)$, noted as

$$\mathcal{F}\{f(t)\} = F(\nu) = \int_{-\infty}^{\infty} f(t) \exp(-j2\pi\nu t) dt. \tag{2.10}$$

In Fourier optics, an arbitrary light wave propagating in free space can be seen as a combination of different plane waves. According to wave optics, a plane wave can be defined as $U(x, y, z) = A \exp[-j(k_x x + k_y y + k_z z)]$, where k_i are components of wavevector $\mathbf{k}$. Assuming that the monochromatic wave propagates in the x-y plane, the two-dimensional Fourier transform of wave $U(x, y)$ can be given by [12]:

$$\mathcal{F}\{U\}(\nu_x, \nu_y) = \iint_{-\infty}^{\infty} U(x, y) \exp[-j2\pi(\nu_x x + \nu_y y)] dx dy \tag{2.11}$$

where $\nu_x = k_x/2\pi$ and $\nu_y = k_y/2\pi$ are the spatial frequencies. In physical terms, each point (ν_x, ν_y) in the Fourier domain corresponds to a plane wave propagating with a specific set of direction cosines.

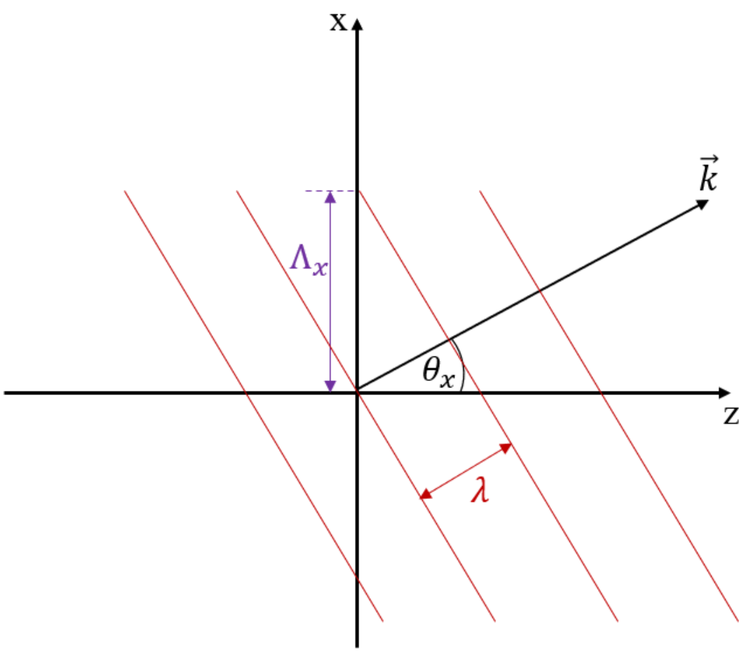

Figure 2.3: The angular decomposition of a plane wave in x-z plane

Considering a plane wave is propagating in x-z plane as illustrated in 2.3, with the spatial period along x-axis $\Lambda_x = 1/\nu_x$ and thus the angle between wavevector **k** and z-axis, $\theta_x = sin^{-1}(k_x/k)$. With the similar decomposition in y-z plane, the relations between different wavenumbers $k = \sqrt{k_x^2 + k_y^2 + k_z^2} = 2\pi/\lambda$ can be defined. If $k_x, k_y \ll k$, the wavevector $\overrightarrow{k}$ can be seen as paraxial, so that the angle θ_x and θ_y are small ($sin\theta_x \approx \theta_x$, $sin\theta_y \approx \theta_y$)[11], and thus the angles can be given by:

$$\theta_i = \lambda \nu_i \tag{2.12}$$

2.2.1 Propagation of light

When light propagates from an initial plane $z = 0$ to another plane at distance z, its evolution can be described by the angular spectrum of plane waves. As established in [11], free space acts as a linear shift-invariant system with a specific transfer function.

If the complex field at $z = 0$ is $U(x, y, 0)$, its angular spectrum $\mathcal{F}\{U\}(\nu_x, \nu_y, 0)$ undergoes a phase shift during propagation. The spectrum at distance z is given by:

$$\mathcal{F}\{U\}(\nu_x, \nu_y, \nu_z) = \mathcal{F}\{U\}(\nu_x, \nu_y, 0) H(\nu_x, \nu_y) \tag{2.13}$$

The transfer function H is defined as:

$$H(\nu_x, \nu_y) = \exp\left(jkz\sqrt{1 - (\lambda\nu_x)^2 - (\lambda\nu_y)^2} \right) \tag{2.14}$$

where $k = 2\pi/\lambda$. For spatial frequencies where $(\lambda\nu_x)^2 + (\lambda\nu_y)^2 > 1$, Equation 2.14 becomes an attenuation factor and the waves become evanescent, meaning free space effectively acts as a low-pass filter that limits the resolution of imaging systems.

2.2.2 Diffraction of light in near-field and far-field

Diffraction is the phenomenon where light waves encounter an aperture and deviate from the shadow of the aperture. The observed diffraction pattern depends significantly on the propagation distance d and the aperture size D.

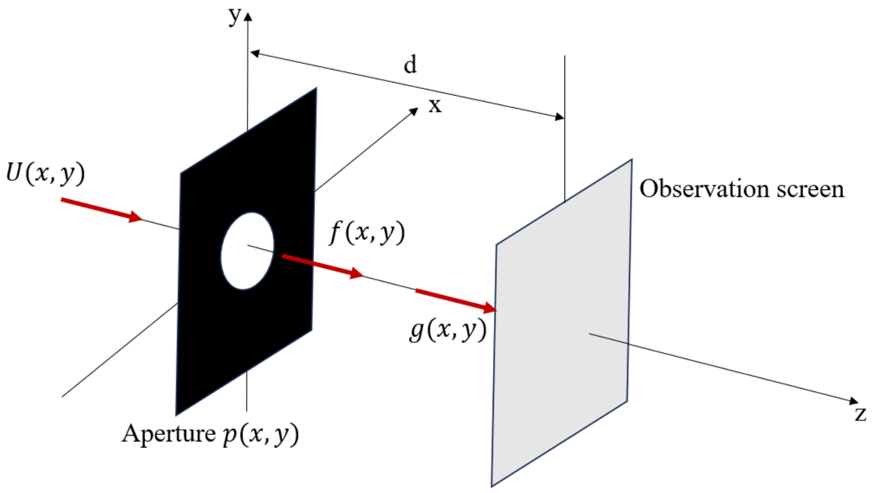

Figure 2.4: Diffraction geometry.

Figure 2.4 shows an incident light wave with complex amplitude $U(x, y)$ transmitting through an aperture to the observation screen at distance d. The complex amplitude after the aperture is given by

$$f(x, y) = U(x, y)p(x, y), \tag{2.15}$$

where $p(x, y)$ is the aperture function.

Fraunhofer diffraction (far-field) and Fourier transform properties of lenses

As discussed above, the diffraction pattern is related to the distance. As the distance z increases such that $d \gg \pi D^2/\lambda$, the complex amplitude at the observation screen can be given by Fraunhofer diffraction:

$$g(x, y) \approx \frac{e^{jkd}}{j\lambda d} \iint f(x, y) \exp\left[-j2\pi(\nu_x x + \nu_y y)\right] dxdy. \tag{2.16}$$

The intensity of the diffraction pattern on the screen $I(x, y) = |g(x, y)|^2$ is

$$I(x, y) = \frac{1}{(\lambda d)^2} \left| \iint f(x, y) \exp\left[-j2\pi(\nu_x x + \nu_y y)\right] dxdy \right|^2. \tag{2.17}$$

Here, using the paraxial approximation $\sin\theta_x \approx \theta_x$, $\sin\theta_y \approx \theta_y$, the k vectors in x-y plane are $k_x \approx (x/d)k$ and $k_y \approx (y/d)k$, and thus the spatial frequencies are $\nu_x = x/\lambda d$ and $\nu_y = y/\lambda d$. Therefore, the diffraction pattern under Fraunhofer approximation is proportional to the Fourier transform of the complex amplitude $f(x, y)$ after the aperture.

To fulfill the far-field condition, for an aperture with diameter $D = 0.8$ mm and incident wavelength $\lambda = 523$ nm, the distance between the aperture and screen should be

$$d \gg \frac{\pi D^2}{\lambda} \approx 3.8 \text{ m} \tag{2.18}$$

However, when an aperture (or mask) is placed in the front focal plane of a lens with focal length f, the complex amplitude distribution in the focal plane can be given by the Fraunhofer diffraction in Equation 2.17 replacing the scale factor to $1/\lambda f$ [11]. Thus, a positive lens can naturally perform a two-dimensional Fourier transform as:

$$I(x_f, y_f) = \frac{1}{(\lambda f)^2} \left| \iint f(x_n, y_n) \exp\left[\frac{-j2\pi}{\lambda f}(x_n x_f + y_n y_f)\right] dx_n dy_n \right|^2, \tag{2.19}$$

where x_n, y_n is the positions in near-field and x_f, y_f are the positions in far-field.

2.3 Optical aberrations and wavefront

2.3.1 Primary aberrations

Aberrations are likely to exist in optical systems and affect the performance, as a result of the design of optical components and the properties of light interacting with curved surfaces. Spatiotemporal couplings (STCs) in an ultrashort laser system can be highly related to the aberrations. In this section, types of primary aberrations will be introduced, and can generally be divided into monochromatic and chromatic aberrations as shown in Figure 2.5.

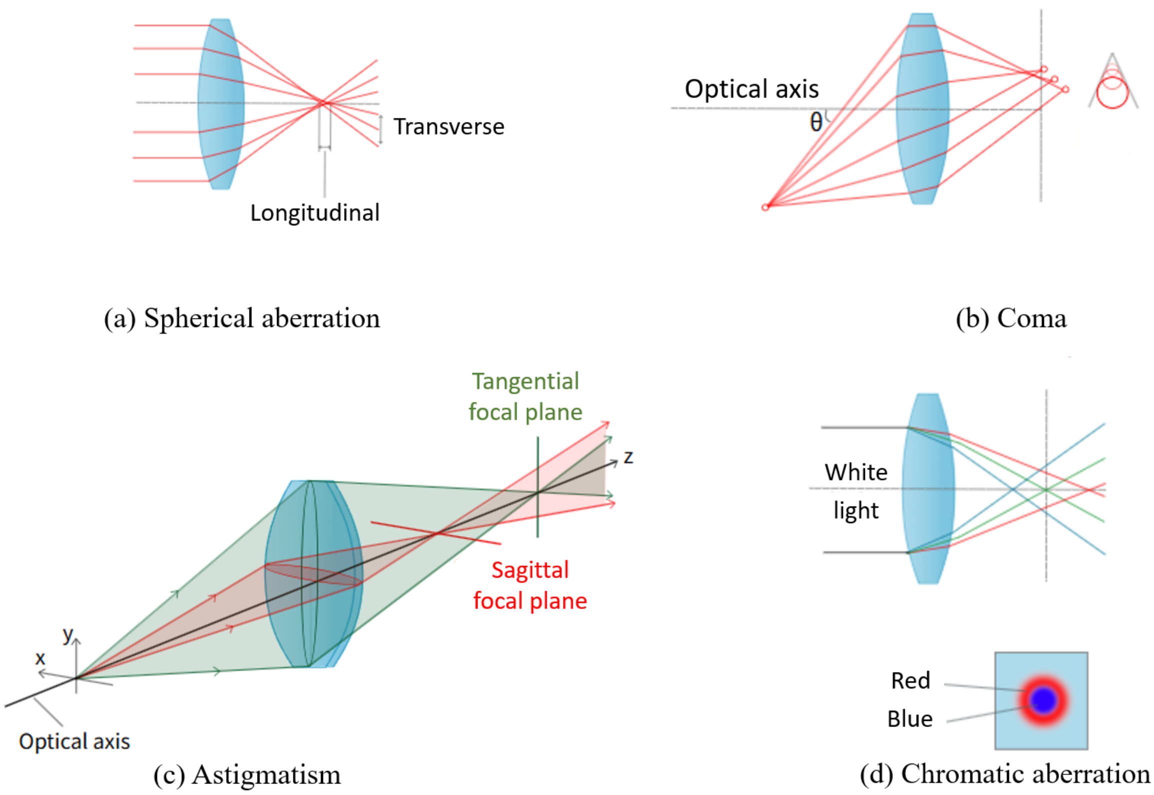

(a) Spherical aberration (b) Coma (c) Astigmatism (d) Chromatic aberration

Figure 2.5: Primary aberrations. (a) Spherical aberration; (b) Coma; (c) Astigmatism; (d) Chromatic aberration. These figures are published in [13]

.

Spherical aberration

Instead of a single sharp focal point, spherical aberration creates a broadened, symmetrically enlarged focal spot. The reason for this is that light rays passing through the outer edges of a spherical mirrors or lens are reflected or refracted differently compared to the rays passing near the center, thus passing through different focal points. To avoid this, one simple method could be using aspheric lenses, but these lenses are difficult to manufacture and more expensive. Another way to correct spherical aberration is to combine convex and concave lenses to compensate the effect.

Coma

Coma is an off-axis optical aberration that arises when a spherical lens exhibits varying transverse magnification across its aperture. When an object is imaged by a lens suffering from coma, light rays passing through the outer edge of the lens produce a differently sized image compared to the rays passing near the center of the lens. The focal spot of the off-axis point appears to be blurry and distorted with a bright core and a fading tail like a comet.

Astigmatism

Astigmatism arises when an optical system exhibits different refractive powers (focal lengths) in two orthogonal planes, typically referred to as the sagittal and tangential planes. Consequently, rays propagating in these different planes focus at different positions along the optical axis. For a laser beam, this transforms a circular beam profile into an elliptical one, with the major axis of the ellipse flipping its orientation by 90 degrees as the beam passes through the focal region.

Chromatic aberration

Unlike monochromatic aberrations, chromatic aberration is dependent on the wavelength of the light source. It is caused by the dispersive property of optical materials, i.e. the refractive index varies with the wavelength. In longitudinal chromatic aberration, different spectral components of the pulse focus at different distances along the propagation axis. For broadband light source, such as ultrashort pulses, chromatic aberration is particularly critical. It is the primary effect that induces spatiotemporal couplings (STCs), such as pulse-front curvature (PFC), because the spatial propagation is linked to the temporal or spectral properties.

2.3.2 Zernike polynomials and wavefront representation

In optical systems, wavefront means the surface of constant phase ϕ for an electromagnetic wave. For an ideal, undisturbed laser beam, the wavefront is a perfectly flat plane or a smooth sphere. However, as the beam propagates through optical elements with aberrations, the wavefront becomes distorted. To quantitatively characterize these distortions, it is necessary to decompose the wavefront into a set of orthogonal basis functions.

For systems with circular apertures, such as most laser beams, Zernike polynomials are the standard mathematical tool for this representation. The Zernike polynomials are orthogonal over the unit circle ($\rho \leq 1$). The wavefront phase $W(\rho, \theta)$ can be expressed as a linear combination of Zernike polynomials $Z_n^m(\rho, \theta)$:

$$W(\rho, \theta) = \sum_{n=0}^{\infty} \sum_{m=-n}^{n} c_n^m Z_n^m(\rho, \theta) \tag{2.20}$$

where $\rho = r/R$ is the normalized radial coordinate ($0 \leq \rho \leq 1$), θ is the azimuthal angle ($0 \leq \theta \leq 2\pi$), c_n^m are the Zernike coefficients, representing the weight of each specific aberration mode and n is the radial degree and m is the azimuthal frequency.

The polynomials are typically defined by a radial part $R_n^{|m|}(\rho)$ and an angular part:

$$Z_n^m(\rho, \theta) = \begin{cases} N_n^m R_n^{|m|}(\rho) \cos(m\theta), & \text{for } m > 0 \\ N_n^m R_n^{|m|}(\rho) \sin(|m|\theta), & \text{for } m < 0 \\ N_n^0 R_n^0(\rho), & \text{for } m = 0 \end{cases} \tag{2.21}$$

A conventional mapping the two indices n, m into a single index j is the OSA/ANSI standard indices:

$$i = \frac{n(n+2)+m}{2}. \tag{2.22}$$

Physical Interpretation of Zernike Terms

The primary advantage of Zernike polynomials is that their lower-order terms correspond directly to classical Seidel aberrations. Table 2.1 is the common Zernike terms and their corresponding aberrations.

Table 2.1: Zernike polynomials and corresponding aberrations.

Z_n^m	OSA/ANSI Index i	Polynomial $Z_i(\rho, \theta)$	Classical Name
Z_0^0	0	1	Piston
Z_1^{-1}	1	$2\rho \sin\theta$	Vertical Tilt (Y-Tilt)
Z_1^1	2	$2\rho \cos\theta$	Horizontal Tilt (X-Tilt)
Z_2^{-2}	3	$\sqrt{6}\rho^2 \sin(2\theta)$	Oblique astigmatism
Z_2^0	4	$\sqrt{3}(2\rho^2 - 1)$	Defocus
Z_2^2	5	$\sqrt{6}\rho^2 \cos(2\theta)$	Vertical astigmatism
Z_3^{-3}	6	$\sqrt{8}\rho^3 \sin(3\theta)$	Vertical trefoil
Z_3^{-1}	7	$\sqrt{8}(3\rho^3 - 2\rho) \sin\theta$	Vertical coma
Z_3^1	8	$\sqrt{8}(3\rho^3 - 2\rho) \cos\theta$	Horizontal coma
Z_3^3	9	$\sqrt{8}\rho^3 \cos(3\theta)$	Oblique trefoil
Z_4^{-4}	10	$\sqrt{10}\rho^4 \sin(4\theta)$	Vertical quadrafoil
Z_4^{-2}	11	$\sqrt{10}(4\rho^4 - 3\rho^2) \sin(2\theta)$	Oblique secondary Astigmatism
Z_4^0	12	$\sqrt{5}(6\rho^4 - 6\rho^2 + 1)$	Primary spherical aberration
Z_4^2	13	$\sqrt{10}(4\rho^4 - 3\rho^2) \cos(2\theta)$	Vertical secondary Astigmatism

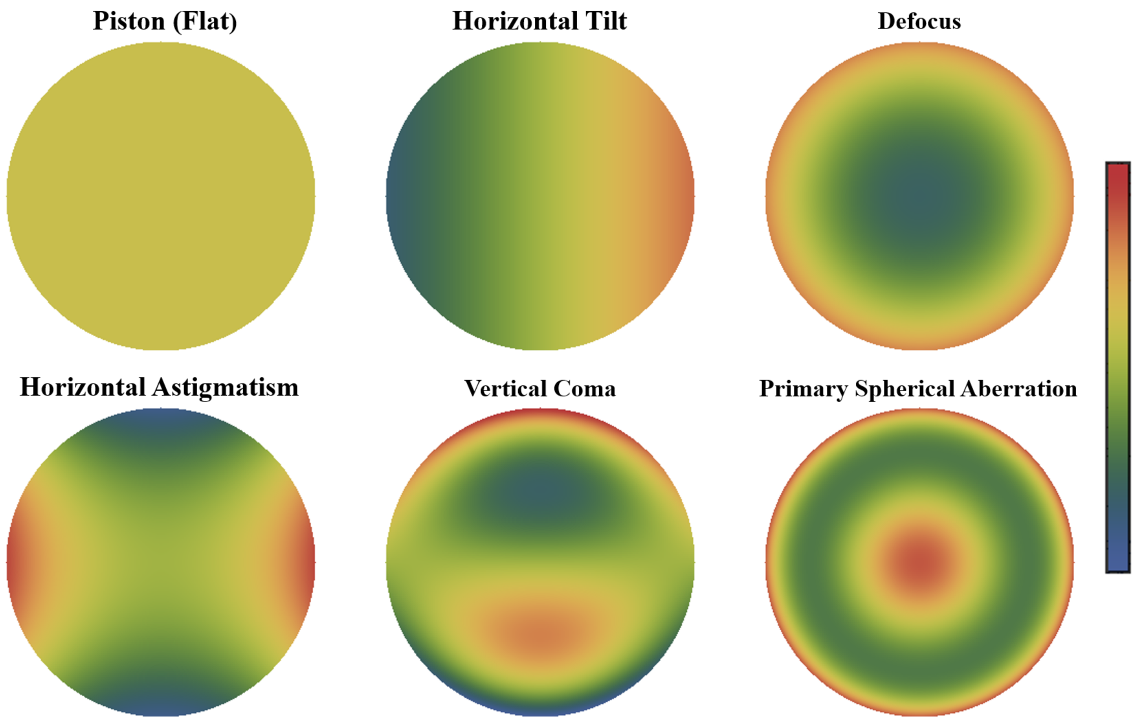

Figure 2.6: Zernike polynomials illustrating fundamental optical wavefront aberrations. The wavefronts are normalized and generated by [14].

In the context of laser beam characterization, the most relevant terms in Figure 2.6 are: Tilt (Z_1^{-1}, Z_1^1), representing a global tilt of the wavefront, which leads to a transverse shift of the focal spot in the focal plane; Defocus (Z_2^0), representing a longitudinal shift of the focus along the optical axis; Astigmatism (Z_2^{-2}, Z_2^2), Coma (Z_3^{-1}, Z_3^1), and Spherical Aberration (Z_4^0), representing higher-order spatial distortions that degrade the focal spot quality and peak intensity.

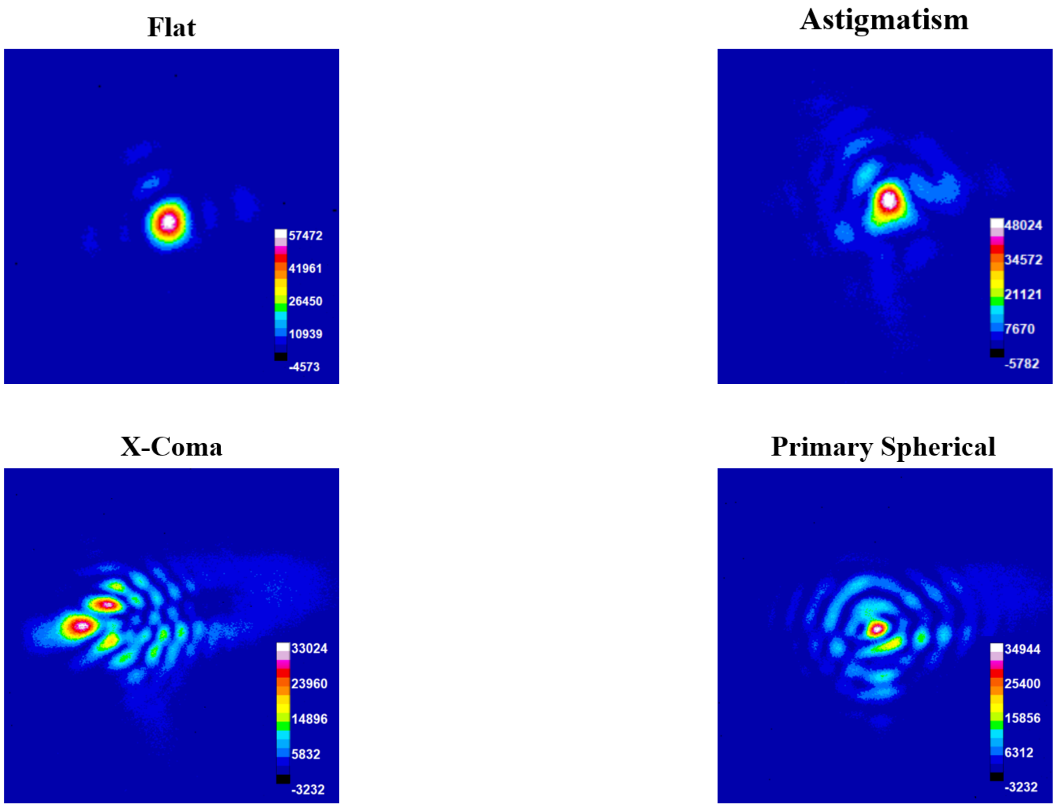

Figure 2.7: Focal spot of the OPCPA laser system with different aberrations.

Figure 2.7 shows the focal spot intensity images when the laser beam is affected by the corresponding aberrations in Figure 2.6 and Table 2.1.

Wavelength Dependence and spatiotemporal couplings

For monochromatic light, the Zernike coefficients c_n^m are constants. However, ultrashort pulses—such as those in the multi-terawatt OPCPA system at LLC—possess a broad spectral bandwidth. Due to the dispersive nature of optical materials (chromatic aberration), the wavefront distortion becomes highly wavelength-dependent. Thus, the wavefront must be described as a function of wavelength λ:

$$W(\rho, \theta, \lambda) = \sum c_n^m(\lambda) Z_n^m(\rho, \theta) \tag{2.23}$$

This wavelength dependence is the fundamental origin of spatiotemporal couplings (STCs). The IMPALA technique aims to diagnose these couplings by retrieving the Zernike coefficients for each spectral component. Pulse-front tilt (PFT) arises if the tilt coefficients ($c_1^{\pm 1}$) vary linearly with wavelength, implying that different frequencies point in different directions (angular dispersion). Pulse-front curvature (PFC) arises if the defocus coefficient (c_2^0) varies with wavelength, meaning different frequencies focus at different longitudinal positions (longitudinal chromatic aberration).

2.4 Spatiotemporal couplings

In multi-terawatt systems relying on chirped pulse amplification (CPA), managing longitudinal dispersion is only part of the challenge. When a pulse with massive spectral bandwidth interacts with optical components that modify both spatial and spectral properties—such as lenses, prisms, and diffraction gratings—its temporal and spatial profiles become inextricably linked or coupled. This phenomenon, where the electric field $E(x, y, t)$ cannot be factored into independent spatial and temporal components, is known as spatiotemporal couplings (STCs) [2]. Two foundational STCs (pulse-front tilt and pulse-front curvature) severely limit the focal intensity in high-power systems.

2.4.1 Pulse-front tilt and angular dispersion

Pulse-front tilt (PFT) occurs when the arrival time of the pulse varies linearly across the transverse spatial coordinate (e.g., the x-axis). Physically, PFT is the direct time-domain manifestation of angular dispersion in the frequency domain. When a broadband beam reflects off a grating or passes through a prism, different wavelength components propagate at slightly different angles $\theta(\lambda)$. Figure 2.8 shows an example where PFT is produced by a grating.

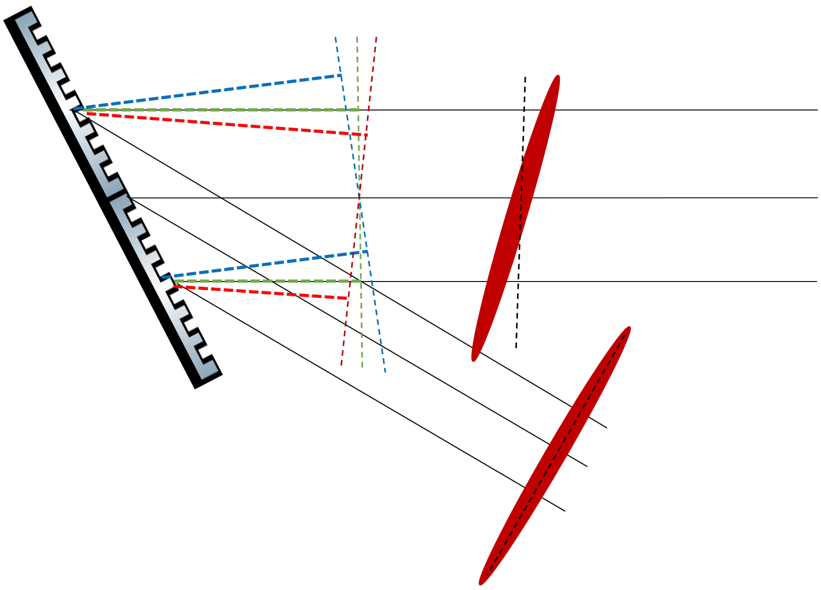

Figure 2.8: Pulse-front tilt is produced by a grating. The phase fronts are shown for different frequencies, and the dash line is the phase front of the average frequency.

According to general STC theory, the relationship between the angular dispersion

$d\theta/d\lambda$ and the group-delay gradient $\Delta\tau_g$ (which characterizes the PFT) can be expressed as:

$$\Delta\tau_g = \frac{\lambda_0}{c}\frac{d\theta}{d\lambda} \tag{2.24}$$

where c is the speed of light and λ_0 is the central wavelength [2]. In a poorly aligned CPA compressor, residual angular dispersion will lead to significant PFT, causing the pulse to smear out in time at the focal plane, thereby destroying the peak intensity.

2.4.2 Pulse-front curvature and chromatic curvature

While PFT involves a linear delay, Pulse-front curvature (PFC) involves a quadratic delay across the beam profile. PFC predominantly arises from the longitudinal chromatic aberration of refractive lenses (as shown in Figure 2.9). Because the refractive index of glass decreases with wavelength in the near-infrared region, a standard convex lens will focus the "blue" (high-frequency) components of the pulse tighter and closer to the lens than the "red" (low-frequency) components.

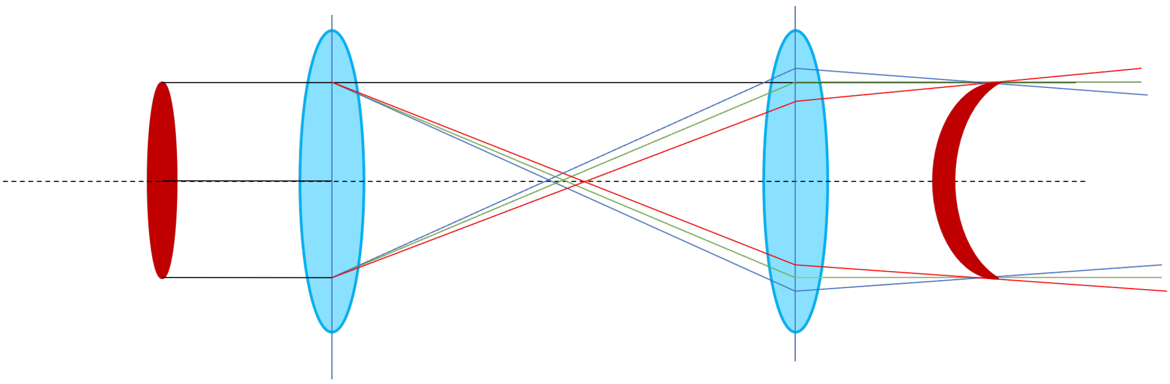

Figure 2.9: Pulse-front curvature introduced by lenses.

In the near field, this means the group delay varies radially, curving the energy front of the pulse. When measuring wavefronts across different spectral slices—as is done in the IMPALA technique—PFC reveals itself as a wavelength-dependent Zernike defocus term (Z_2^0). Successfully diagnosing and correcting these couplings is the ultimate goal of characterizing the terawatt OPCPA laser system.

3 Gerchberg-Saxton algorithms

In optical experiments, sensors such as CCD or CMOS cameras can only record the time-averaged intensity of a light field, $I(x, y) = |U(x, y)|^2$. The phase information, which is crucial for complete characterization of the wave and wavefront reconstruction, is inherently lost during the measurement process. Retrieving this missing phase from intensity measurements is a fundamental problem known as phase retrieval.

Proposed by Robert W. Gerchberg and Walter O. Saxton in 1972 [15], the Gerchberg-Saxton (GS) algorithm is an iterative computational method utilized to reconstruct the phase of a complex wave field from two intensity distributions recorded at two different planes, i.e. the object (near-field) plane and its corresponding Fourier (or far-field) plane. It is shown that the GS algorithm indeed has a unique solution to the phase retrieval problem through the iterative process [16]. As demonstrated in section 2.2, the relationship between these two planes can be optically realized using a positive lens, making the fields a Fourier transform pair.

3.1 Principle of the algorithm

Let the complex amplitude in the object plane (e.g., the mask or aperture plane) be defined as $f(x, y) = a_0(x, y) \exp[j\phi(x, y)]$, where $a_0(x, y)$ is the known or measured amplitude distribution and $\phi(x, y)$ is the unknown phase to be retrieved. The corresponding complex amplitude in the Fourier plane is given by

$$G(\nu_x, \nu_y) = A_0(\nu_x, \nu_y) \exp[j\psi(\nu_x, \nu_y)], \tag{3.1}$$

where $A_0(\nu_x, \nu_y)$ is the measured far-field amplitude obtained from the intensity pattern, and thus $A_0 = \sqrt{I_f}$.

The process of the standard GS algorithm is shown in Figure 3.1. The algorithm iterates between the spatial and spatial frequency domains, enforcing the known intensity constraints at each step while preserving the phase estimated from the previous step.

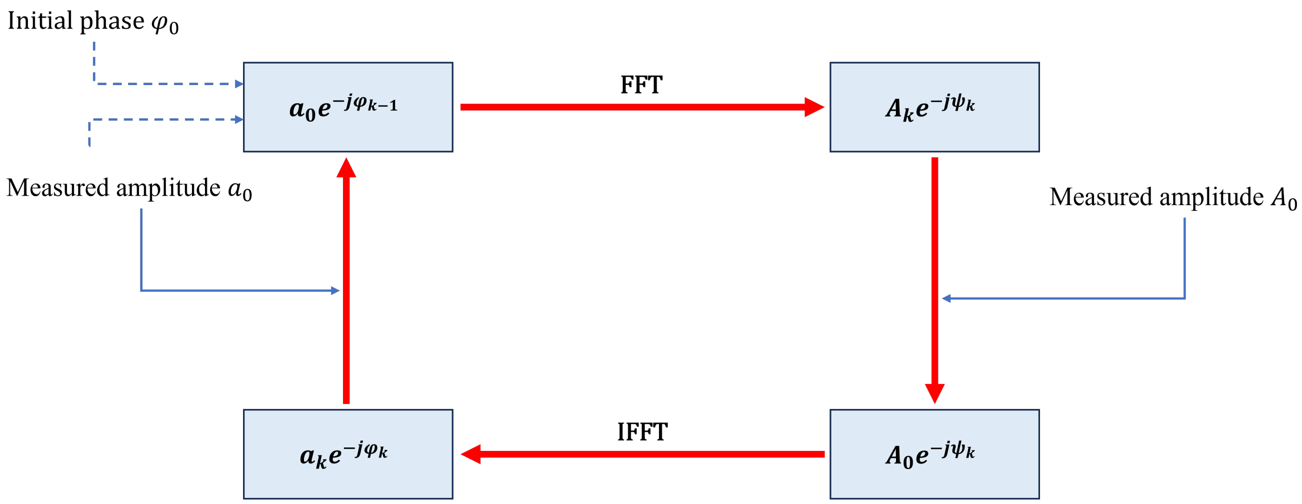

Figure 3.1: Block diagram of the iterative process in the standard Gerchberg-Saxton algorithm for the k-th iteration.

Assuming an initial random phase guess $\phi_0(x, y)$ uniformly distributed between $-\pi$ and π, the k-th iteration of the GS algorithm consists of several sequential steps.

First, the complex field in the object plane is Fourier transformed to estimate the field in the Fourier domain:

$$G_k(\nu_x, \nu_y) = \mathcal{F}\{a_0(x, y) \exp[j\phi_{k-1}(x, y)]\} = A_k(\nu_x, \nu_y) \exp[j\psi_k(\nu_x, \nu_y)], \tag{3.2}$$

where A_k and ψ_k are the calculated amplitude and phase, respectively.

Next, a constraint will be applied to the Fourier domain. The calculated amplitude $A_k(\nu_x, \nu_y)$ is replaced by the actual measured amplitude $A_0(\nu_x, \nu_y)$, while keeping the calculated phase ψ_k unchanged. This forms the updated Fourier field:

$$G'_k(\nu_x, \nu_y) = A_0(\nu_x, \nu_y) \exp[j\psi_k(\nu_x, \nu_y)]. \tag{3.3}$$

Then an inverse Fourier transform is applied to G'_k to propagate the field back to the object plane:

$$f'_k(x, y) = \mathcal{F}^{-1}\{G'_k(\nu_x, \nu_y)\} = a_k(x, y) \exp[j\phi'_k(x, y)]. \tag{3.4}$$

Lastly, the calculated amplitude $a_k(x, y)$ is replaced by the known object amplitude $a_0(x, y)$ (e.g., the transmission profile of the pinhole mask), yielding the updated field for the next iteration:

$$f_{k+1}(x, y) = a_0(x, y) \exp[j\phi'_k(x, y)]. \tag{3.5}$$

The new phase estimate for the next loop becomes $\phi_{k+1}(x, y) = \phi'_k(x, y)$.

3.2 Convergence and error

The iteration process continues until the calculated amplitude A_k converges to the measured target amplitude A_0. To monitor the convergence, the mean square error

(MSE) is commonly evaluated at each step in the Fourier domain [17]:

$$E_k^2 = \frac{\iint |A_k(\nu_x,\nu_y) - A_0(\nu_x,\nu_y)|^2 \, d\nu_x d\nu_y}{\iint |A_0(\nu_x,\nu_y)|^2 \, d\nu_x d\nu_y} \tag{3.6}$$

A fundamental property of the GS algorithm is that the error E_k^2 monotonically decreases or remains constant with each iteration. Once E_k^2 drops below a predefined tolerance threshold, the algorithm is terminated, and the final $\phi_k(x, y)$ is accepted as the retrieved wavefront phase. In practical applications such as the IMPALA technique, this iterative phase retrieval method will provide a stable way to reconstruct wavefront aberrations solely from far-field speckle intensity patterns. However, there are still convergence challenges in the GS algorithm. These challenges arise from the tendency of the algorithm to stagnate in a local minimum value, where iterations cease to reduce the error significantly without reaching the global optimum. This stagnation can be obvious in cases with centrosymmetric support constraints. These issues stem from the algorithm's reliance on iterative projections onto non-convex constraint sets, leading to entrapment rather than progression toward the true solution [18]. The algorithm is also sensitive to the initial phase guess and noises in the input intensity measurements. Thus, running several trials and selecting the best outcome are often required to mitigate inconsistent results [19].

3.3 Improvements of the standard GS algorithm

There are many different improvements and modifications to the standard GS algorithm that have been developed.

3.3.1 Spatial phase perturbation (SPP) GS algorithm

The SPP-GS algorithm addresses the stagnation problem by introducing extra phase perturbations to the object field during iterations. By applying a spatially varying, pseudo-random phase mask in the spatial domain, the algorithm is forced out of local traps in the error landscape [20]. This perturbation helps the field traverse a larger volume of the phase space, significantly increasing the probability of finding the global optimum.

3.3.2 Double-phase retrieval (DPR) algorithm

The DPR algorithm involves two different intensity distributions I_1 and I_2 recorded at different planes (usually at the object plane and the far-field image plane). By performing iterative projections between the two intensity constraints, the DPR algorithm resolves the reconstruction of twin images that often plagues single-plane phase retrieval [21, 22]. This method is particularly effective for systems where the phase varies significantly across the aperture.

3.3.3 Multiple-phase retrieval (MPR) algorithm

Expanding on the multi-plane concept, the MPR algorithm utilizes a sequence of intensity measurements taken along the propagation axis [21]. By enforcing constraints at N different planes, the MPR algorithm effectively performs a "soft" optimization of the error function. The inclusion of redundant data provides superior noise robustness and enables the retrieval of high-fidelity phases even in the presence of strong aberrations [17].

The selection of an appropriate algorithm depends on the experimental complexity; while SPP-GS is ideal for simple iterative setups, multi-plane methods like MPR are preferred when high precision is required for characterization of complex wavefronts.

3.3.4 Hybrid input-output (HIO) algorithm

Beyond multi-plane methods, the hybrid input-output (HIO) algorithm represents a significant leap in retrieval robustness. Introduced by Fienup [17], the HIO algorithm modifies the spatial domain projection to avoid stagnation. Instead of a direct replacement of the spatial field, it utilizes a feedback parameter β to update the field based on the violation of the object domain constraints. This allows the algorithm to explore the phase space more efficiently, making it highly effective for reconstructing wavefronts with complex supports or non-trivial boundaries.

4 Method

4.1 Experimental setups

The iterative phase-retrieval technique was tested using two different laser systems. The initial test and data processing program development was done using the fiber-coupled diode laser, delivering continuous-wave (CW) laser beam of 523 nm. Then, the high-power terawatt laser in LLC was used to deliver ultrashort pulses and to characterize the wavefront using this technique. Moreover, the deformable mirror (DM) inside the system was also used to deliberately introduce aberrations to the wavefront, so as to analyze the performance of the IMPALA technique as well as the Gerchberg-Saxton algorithm.

4.1.1 Fiber-coupled diode laser

The emission of continuous laser light from a fiber-coupled diode laser originates from the semiconductor chip, which typically acts as a Fabry-Perot cavity, while the optical fiber serves as a passive delivery medium. Several longitudinal modes, or standing waves, can exist within the semiconductor cavity simultaneously. For a diode cavity with physical length L and effective refractive index n_{eff}, the possible frequencies of these standing waves are determined by [23]:

$$\nu = \frac{c}{2n_{\text{eff}}L} \cdot n, \quad n = 1, 2, ... \tag{4.1}$$

where c is the speed of light in vacuum. The semiconductor gain medium has a broad gain profile, so the actual laser output is a weighted sum of the longitudinal modes that fall within this envelope, which is subsequently coupled into the optical fiber.

The frequencies of these longitudinal modes depend on the optical path length of the diode cavity, $n_{\text{eff}}L$. Fiber-coupled diode lasers are extremely sensitive to thermal perturbations. This thermal instability is particularly obvious when the laser is initially switched on. As the semiconductor junction heats up, both the physical length of the cavity and its refractive index change (thermal drift). This causes the densely packed longitudinal modes to shift and wander across the gain envelope. Depending on where the modes are positioned under the temperature-dependent gain profile, the output wavelength and power will experience slight variations until the diode reaches thermal equilibrium.

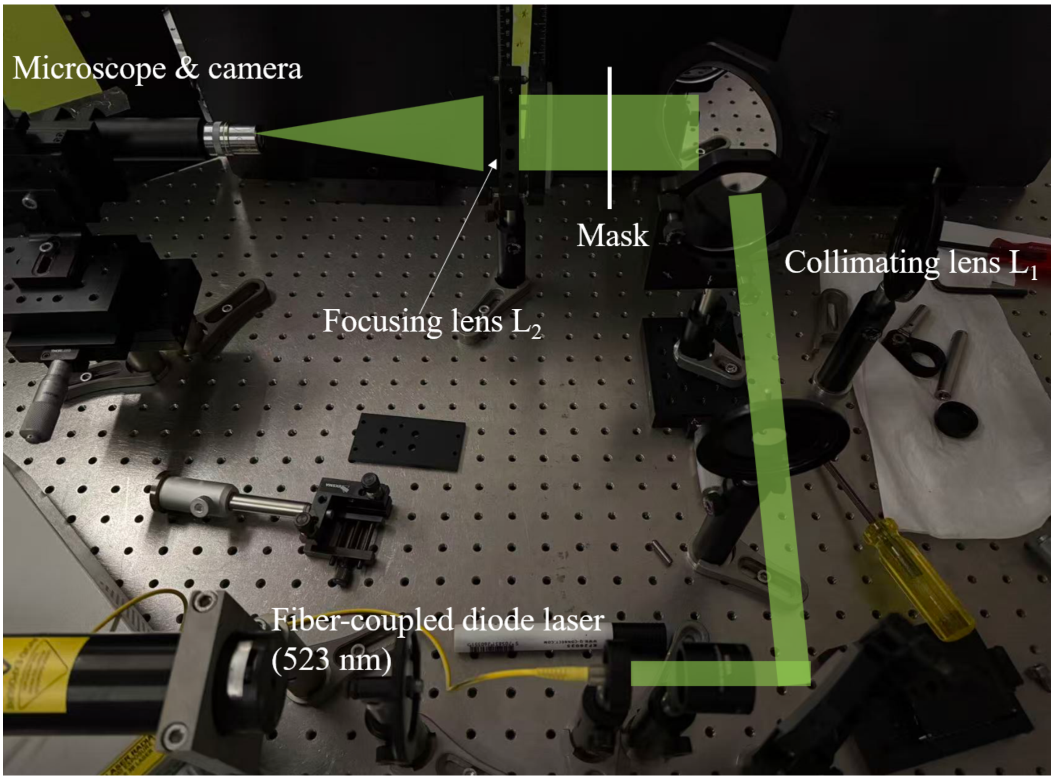

Figure 4.1: Fiber-coupled diode laser setup, with two lens of 400 mm and 200 mm to expand and focus the beam, a camera of 2048 × 3072 pixels (2.4 μm per pixel) connected to a 10x magnification microscope and a mask placed before the focusing.

Figure 4.1 shows the basic setup of the fiber-coupled diode laser system. The beam from the fiber-coupled diode laser of 523 nm will first pass through a continuously variable natural density(ND) filter to modulate the light intensity. Then, because of the divergent angle from the fiber, the beam is aligned with the lens L_1 of focal length 400 mm and the beam size can be controlled by an iris before the lens. After bending the beam by a reflecting mirror, the parallel beam will pass through the mask and then be focused by the lens L_2 of focal length 200 mm. For the 523 nm beam and the hole diameter $D = 0.8$ mm, the size of the diffraction pattern d on the focal spot can be calculated as:

$$d = \frac{2.44\lambda f}{D} = \frac{2.44 \times 523 \times 10^{-9} \times 0.2}{0.8 \times 10^{-3}} \approx 0.32 \text{ mm}$$

Then, the pixel numbers for imaging this size is 0.32 mm/2.4 μm = 133, which could be very small in the image and have low resolution. Thus, in the experiment, a microscope of 10x magnification is applied in front of the camera.

4.1.2 The multi-terawatt laser system

The block diagram of the current multi-terawatt laser system at Lund Lund Laser Centre is illustrated in Figure 4.2. The system relies on optical parametric chirped pulse amplification (OPCPA) to deliver extremely broadband, sub-10 fs pulses. The system operates at a repetition rate of 10 Hz, providing pulses with a central wavelength around 850 nm, and an energy of 250 mJ.

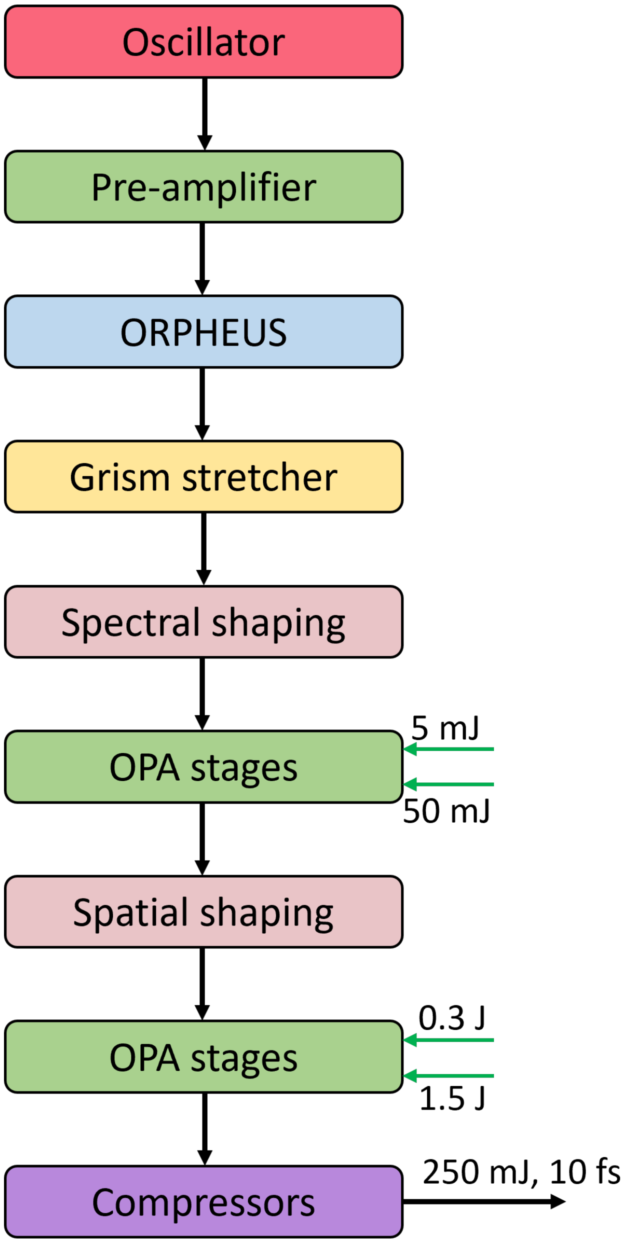

Figure 4.2: Block diagram of the OPCPA laser system, simplified from [24]. The pump lasers (frequency doubled Nd:YAG lasers) in picosecond are showed in green arrows.

In contrast to conventional Titanium:sapphire amplifiers that rely on population inversion and stimulated emission, the OPCPA technique utilizes three-wave mixing inside a non-linear beta-barium borate (BBO) crystal. In this process, energy is coherently transferred from a picosecond pump beam to the signal beam without intermediate energy storage in the crystal. This lack of population inversion significantly suppresses amplified spontaneous emission, leading to an enhanced temporal contrast [24]. The amplified bandwidth is determined by the phase-matching conditions over the crystal length, enabling a broad, spectrum ranging from 750 nm to 1000 nm (as shown in Figure 4.3).

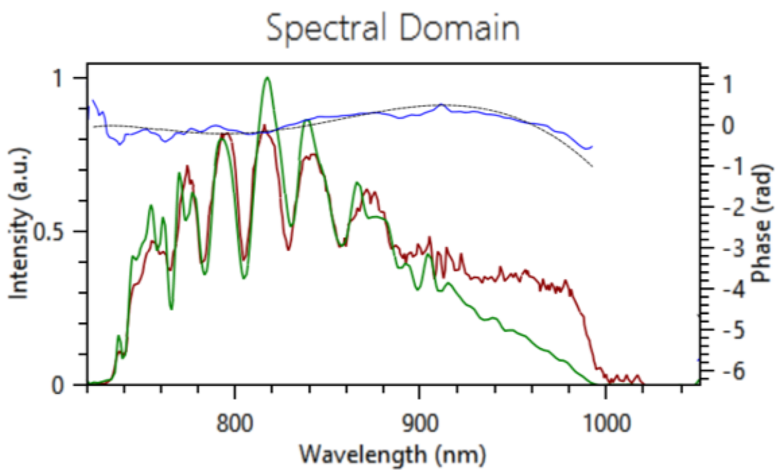

Figure 4.3: OPCPA spectra from d-scan retrieval results. Red line: Measured linear spectrum. Green line: Retrieved linear spectrum. Blue line: Retrieved spectral phase. Black line: 4th order polynomial fit of the spectral phase.

Due to the massive spectral bandwidth, the OPCPA system employs a grism stretcher with negative group delay dispersion to stretch the seed pulses to 60 ps. The system also features a specialized front-end ORPHEUS module to support few-cycle pulses and precise control. This module spectrally broadens the pulse via self-phase modulation and provides passive carrier-envelope phase (CEP) stability through difference-frequency generation (DFG), which cancels the random CEP fluctuations originating from the oscillator [24]. After spectral shaping, the pulse (signal) is then amplified in four consecutive OPA stages, pumped by picosecond Nd:YAG lasers. Finally, the pulse is compressed to approximately 9 fs with energy 250 mJ.

In the IMPALA measurement using the multi-terawatt laser system, the beam was attenuated by an ND 2 filter to avoid saturating the camera. The different IMPALA masks were placed before getting focused by the 4 inch off-axis parabolic mirror with an apparent focal length of 445 mm.

4.2 The IMPALA masks

The IMPALA masks generalize broadband double-slit interferometry and diffraction to a multi-pinhole configuration [9]. By placing a specially designed mask before a focusing optic, an ultrashort laser pulse is split into multiple beamlets. These beamlets interfere at the focal plane (far-field), generating a speckle or streak pattern. In the spatial fast Fourier transform (FFT) of the far-field interference pattern, different spectral components are naturally disperse along radial streaks as shown in Figure 4.4.

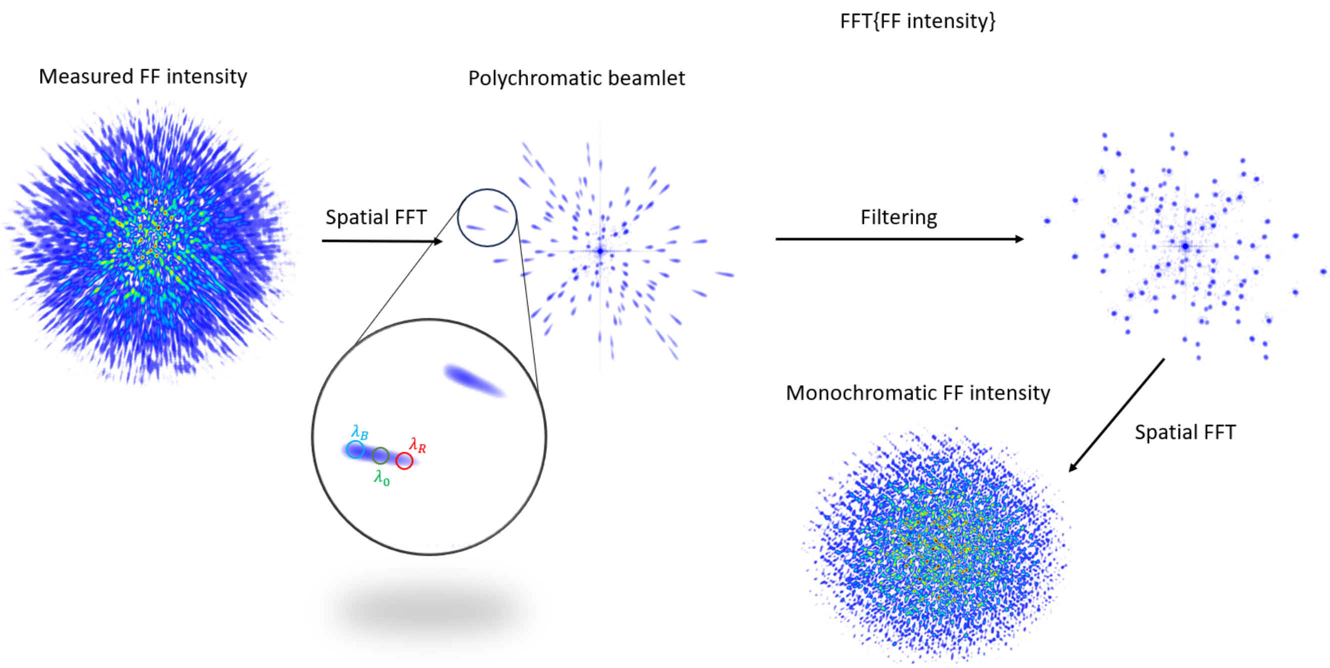

Figure 4.4: Extraction process of the monochromatic far-field intensity, from the radial separation of different wavelengths in Fourier domain.

4.2.1 Mathematical Derivation

Consider two beamlets from the mask with two holes, a reference beamlet at the center and a test beamlet separated by a distance x_1. In the narrow-bandwidth approximation, their interference at the far-field (focal plane coordinate ξ) yields an intensity distribution $I_f(\xi)$ governed by a cosine modulation [10]:

$$I_f(\xi) \propto \exp\left(-\frac{\sigma_0^2\omega_c^2}{c^2f^2}\xi^2\right) \times \left[\underbrace{\frac{1+R^2}{2}}_{DC} + R\exp\left(-\frac{c_B^2}{4}\left(\tau_1+\xi\frac{x_1}{cf}\right)^2\right)\cos\left(\omega_c\left[\tau_1+\xi\frac{x_1}{cf}\right]\right)\right] \tag{4.2}$$

where f is the focal length of the optic, c is the speed of light, $\omega_c = 2\pi c/\lambda$ is the central angular frequency with a bandwidth c_B, x_1 is the spatial separation between the two beamlets in NF plane, σ_0 is the spatial width of the beamlets, ξ represents the spatial coordinate in the FF focal plane, τ_1 is the relative group delay between the beamlets, and DC represents the DC background terms.

Applying a spatial Fourier transform to the far-field intensity $I_f(\xi)$ maps the signal into the spatial-frequency domain (reciprocal coordinate k_ξ). The cosine term will generate a DC peak and two sidebands. The amplitude peaks of these sidebands are located where the argument of the envelope maximizes, which is defined by:

$$|cfk_\xi \pm \omega_c x_1| = 0 \tag{4.3}$$

Solving for the spatial frequency k_ξ yields:

$$k_\xi = \pm\frac{\omega_c x_1}{cf} \tag{4.4}$$

By substituting $\omega_c = 2\pi c/\lambda$, we establish the direct relationship between the spatial frequency position and the wavelength:

$$k_\xi = \pm\frac{2\pi x_1}{\lambda f} \tag{4.5}$$

This shows that the spatial frequency k_ξ is inversely proportional to the wavelength λ ($k_\xi \propto 1/\lambda$). For longer wavelengths (redder), larger λ results in a smaller $|k_\xi|$. Thus, redder spectral components are located closer to the DC center in the FFT plane. For shorter wavelengths (bluer), smaller λ results in a larger $|k_\xi|$. Bluer components are distributed further away from the center.

This radial dispersion stretches the broadband interference signal into continuous streaks in the Fourier plane, allowing monochromatic information to be isolated using digital spatial filters.

4.2.2 Spectral Resolution Limit

The spectral resolution $\Delta\lambda_{impala}$ that can be achieved through this streak-filtering technique depends on both the bandwidth of the pulse and the geometrical parameters of the mask. It is given by [9]:

$$\Delta\lambda_{impala} \approx \Delta\lambda \left(1 + \left[\frac{\Delta\lambda s_b}{\sqrt{2\log 2}\lambda_0 d}\right]^2\right)^{-1/2} \tag{4.6}$$

where $\Delta\lambda$ is the FWHM of the laser spectrum, λ_0 is the central wavelength, s_b is the separation distance between the beamlets (pinholes) in the near-field and d is the diameter of the pinholes.

For typical experimental parameters (e.g., $\Delta\lambda \approx 30$ nm, $\lambda_0 = 770$ nm, $s_b = 12$ mm, and $d_b = 150$ μm), this yields a spectral resolution of approximately 10 nm for the longest streaks.

4.3 Mask design and implementation

To ensure the successful retrieval of the phase using the GS algorithm, the interference sidebands, which appear as streaks in the broadband case, in the spatial Fourier plane should not overlap. To achieve this, the pinhole arrangement of the mask is optimized utilizing the genetic algorithm. Apart from avoiding the overlap, the design is also constrained to ensure the pinholes cover the beam as much as possible to accurately sample the near-field wavefront. The mask samples (Figure A.1) used in this project are designed and fabricated by Weizmann Institute of Science. A single-shot measurement yields the phase at the discrete locations of the pinholes. To achieve higher resolution, the mask is designed to be rotated. By rotating the mask over a series of angular positions (e.g., 12 distinct rotations), denser spatial sampling of the near-field wavefront is obtained, allowing for highly detailed Zernike decomposition of the aberrations.

4.3.1 Mask with 12 pinholes (Mask 1)

The IMPALA mask with 12 pinholes is illustrated in 4.5. The measurement through this mask does not require rotation, which means it can be a single shot measurement. The phase of these pinholes will be retrieved from the GS algorithm. For this mask the

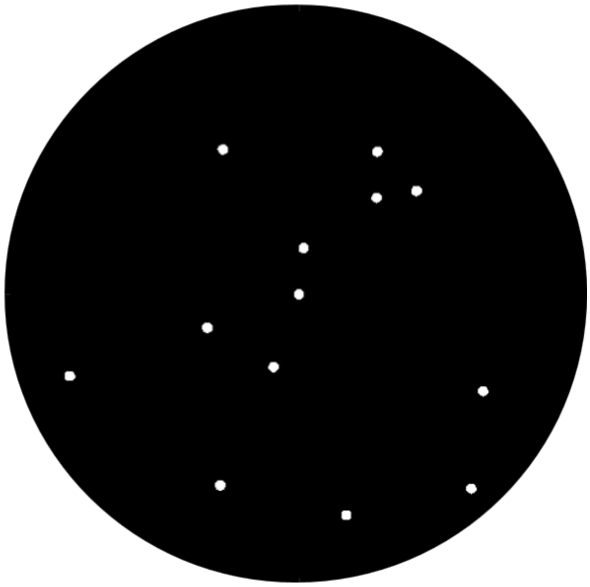

Figure 4.5: Pinholes distribution of the mask with 12 pinholes

largest beamlets' separation $s_b = 32.4$ mm, and the diameter $d_b = 0.8$ mm. Recalling Equation 4.6, the spectral resolution for the longest streak is $\Delta\lambda_{impala} \approx 18.4$ nm.

4.3.2 Mask with 10 pinholes (Mask 2)

For the IMPALA mask with 10 pinholes (Figure 4.6), a single-shot measurement yields the phase at the discrete locations of the pinholes. To achieve higher resolution, the mask is designed to be rotated. By rotating the mask over a series of angular positions (here are 12 rotations, 30 degree each), denser spatial sampling of the near-field wavefront is obtained, allowing for higher orders of Zernike decomposition of the aberrations. As for this mask the largest beamlets' separation $s_b = 34.4$ mm, and the diameter $d_b = 0.8$ mm. The spectral resolution for the longest streak is $\Delta\lambda_{impala} \approx 20.11$ nm.

4.4 Data processing

After passing through the mask and focusing optics, the beamlets will converge and the diffraction pattern on the focal plane, which we consider as far field, will be captured by the camera. This far-field intensity includes the diffraction patterns of different wavelengths from the broadband pulse. Thus, the first step of the data processing is to isolate the monochromatic far-field intensity by applying a digital filter. Then,

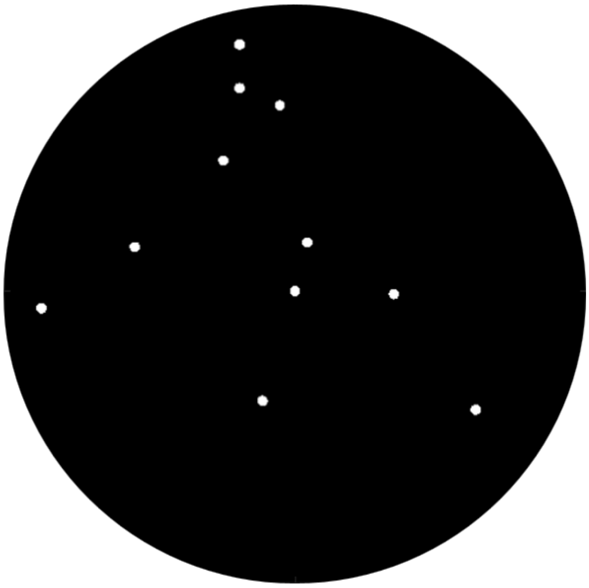

Figure 4.6: Pinholes distribution of the mask with 10 holes

the next step is to retrieve and analyze the near-field phase for each of the isolated wavelengths by GS algorithm.

4.4.1 Filter design

As discussed in the theoretical framework of the IMPALA method, different spectral components of a broadband pulse disperse radially in the spatial-frequency domain (Fourier plane). Because the spatial frequency is inversely proportional to the wavelength, i.e. $\nu \propto 1/\lambda$, it is possible to isolate a specific monochromatic far-field intensity by applying a filter. This subsection will introduce the mathematical and algorithmic principles behind the digital bandpass filter designed to extract a specific target wavelength.

Basic principles

The design process consists of three core steps: calculating the precise target frequency coordinates, applying localized Gaussian windows, and preserving the DC component.

The design of the digital filter starts with mapping physical coordinates to spatial frequencies. For an array of N pinholes, interference occurs between every unique pair of holes (i, j). To extract the interference pattern for a specific target wavelength λ_{target}, the algorithm first predicts the exact location of the resulting sidebands in the Fourier plane.

Based on the far-field diffraction model, the spatial frequencies (ν_x, ν_y) on the CCD sensor are governed by the relative distance between the holes ($\Delta x = x_i - x_j$, $\Delta y = y_i - y_j$), the focal length f, and the effective magnification of the microscope objective

M_{eff}. The target spatial frequencies are calculated as:

$$\nu_x(i,j) = \frac{x_i - x_j}{\lambda_{\text{target}} \cdot f \cdot M_{\text{eff}}}, \qquad \nu_y(i,j) = \frac{y_i - y_j}{\lambda_{\text{target}} \cdot f \cdot M_{\text{eff}}} \tag{4.7}$$

In the programmatic implementation, the pinhole coordinates are first multiplied by a rotation matrix $R(\theta)$ to correct for any experimental angular misalignment before calculating the relative distances. The algorithm iterates through all $N(N-1)$ kinds of combinations of hole pairs to locate all corresponding sideband centers for λ_{target}.

Construction of the Gaussian bandpass filter

Once the theoretical center of a sideband is identified at (ν_x, ν_y), a Gaussian window is applied around this coordinate to extract the signal. The window function $W_{i,j}(\nu_x, \nu_y)$ is defined as:

$$W_{i,j}(\nu_x, \nu_y) = \exp\left(-\frac{(\nu_x - \nu_x(i,j))^2 + (\nu_y - \nu_y(i,j))^2}{2\sigma_k^2}\right) \tag{4.8}$$

Here, the parameter σ_k acts as a spectral bandwidth limiter. A smaller σ_k (a smaller window) extracts a more purified and near-monochromatic signal but restricts high-frequency spatial features, which may lead to ringing artifacts during the inverse Fourier transform. Instead, a larger σ_k accepts a broader spectral sample (reducing spectral resolution) but preserves more spatial structure. The global interference filter mask is generated by the superposition of all individual windows:

$$Mask_{\text{sb}}(\nu_x, \nu_y) = \sum_{i=1}^{N} \sum_{j \neq i}^{N} W_{i,j}(\nu_x, \nu_y) \tag{4.9}$$

Another requirement for retrieving the absolute intensity via the inverse Fourier transform is the preservation of the zero-frequency component which is the central DC peak in the Fourier plane. The DC peak contains the non-interfering baseline intensity of all beamlets. Without it, the reconstructed image would feature non-physical negative intensities. To achieve this, a broader Gaussian window is placed at the origin $(0,0)$ to extract the DC component:

$$W_{\text{DC}}(\nu_x, \nu_y) = \exp\left(-\frac{\nu_x^2 + \nu_y^2}{2(2\sigma_k)^2}\right) \tag{4.10}$$

The final composite filter mask is the sum of the AC and DC masks (capped at a maximum transmission of 1):

$$Mask_{\text{Filter}} = Mask_{\text{sb}} + W_{\text{DC}} \tag{4.11}$$

By multiplying the complex spatial FFT of the raw experimental far-field intensity by $Mask_{\text{Filter}}$, all frequency components corresponding to wavelengths other than λ_{target} are heavily attenuated. An inverse 2D fast Fourier transform of this filtered spectrum subsequently yields the monochromatic far-field intensity distribution $I_{\text{mono}}(\lambda_{\text{target}})$, which will serve as the amplitude input for the GS algorithm to retrieve the spectrally resolved wavefront.

Calibration of the filter

Although the magnification of the microscope objective is known, there are still some misalignment between the actual experimental system and the ideal one. The first misalignment to calibrate is the effective magnification of the system. This effect can be caused by the slightly shift of the camera position around the focal spot, and also by the microscope objective which is connected through a tube with the camera. Another misalignment is the small angular rotation, which can be the effect from the mask when fixing it in the system or rotation of the camera sensor.

The calibration can be done through utilizing an optical bandpass filter. The bandpass filter used for this calibration transmits 830 nm lights, and the FWHM bandwidth of it is 10 nm. Then, the camera will record this measurement in the initial position of the mask (if the mask needs to be rotate). Figure 4.7 shows the distributions of the spatial frequencies of 830 nm on the streaks caused by the radial dispersion effect of the broadband light source in Fourier plane. Based on this, effective magnification and the angular rotation matrix $R(\theta)$ of the filter ($\lambda_{\text{target}} = 830$ nm) will be calibrated, until the filter windows are centered on the locations of spatial frequencies of 830 nm.

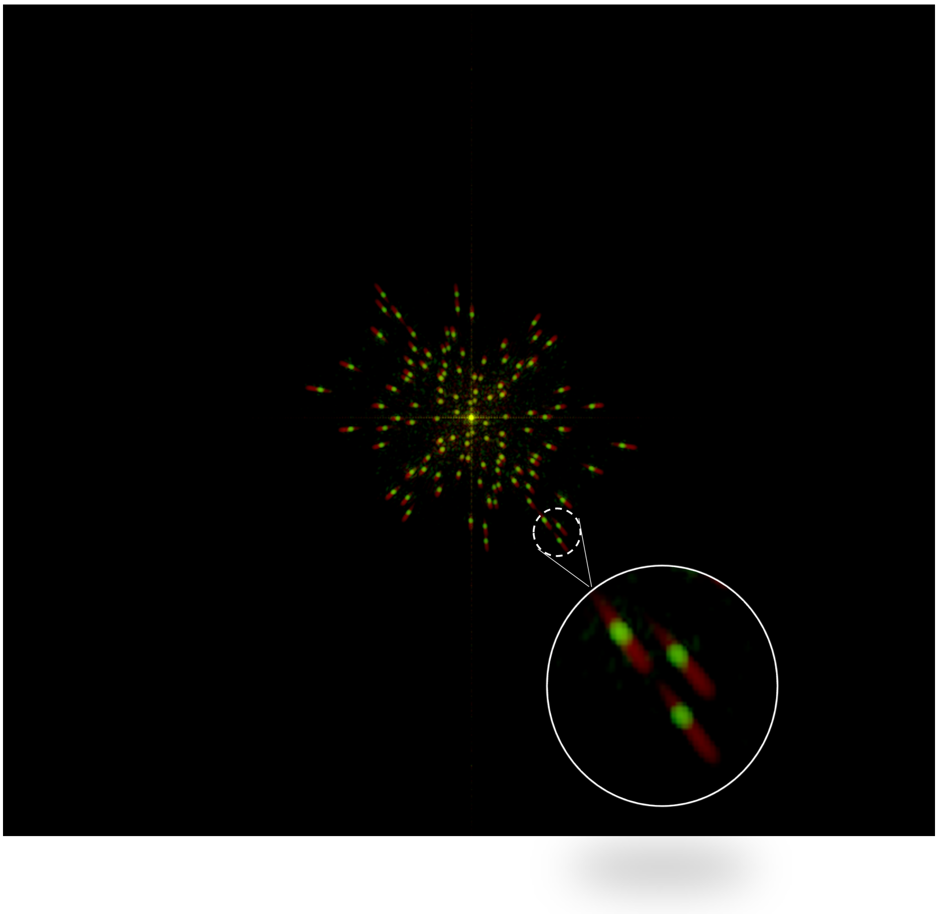

Figure 4.7: Far-field intensity of the multi-terawatt OPCPA laser system with 830 nm($\pm$ 10 nm) bandpass filter merged with the far-field intensity without bandpass filter in Fourier plane. The green spots represent location of spatial frequencies of 830 nm. The red streaks come from the radial dispersion of the broadband pulse in Fourier plane.

After the calibration, the effective magnification of the filter turns out to be $M_{\text{eff}} = 4.05$, and the rotation angle is -3 degree. The implementation of isolating monochromatic far-field intensity using this digital filter is shown in Figure A.2.

4.4.2 Implementation of the GS algorithm

The standard Gerchberg-Saxton (GS) algorithm is used in this project to find the phase from the measured focal spots. Our program uses the basic iterative method between the near field and the far field, instead of complex versions like the Hybrid Input-Output (HIO) algorithm.

A GS algorithm loop of the actual program is shown in Figure 4.8. Before starting the iterations, we set up two main constraints. First, we create a digital mask that matches the real positions of the pinholes. This mask acts as the near-field constraint. Second, the far-field amplitude is calculated by taking the square root of the measured intensity. The camera pixel size does not naturally match the fast Fourier transform (FFT) grid. Therefore, it is necessary to interpolate the measured amplitude to match the native FFT grid exactly. Specifically, the spatial resolution of the native FFT grid is fundamentally determined by the wavelength λ, the focal length f, and the physical length of the computational window L, defined as $\Delta x_{native} = \lambda f/L$. The measured amplitude on the camera sensor grid is mapped onto this native grid using a 2D linear interpolation algorithm. This interpolated amplitude becomes the far-field constraint.

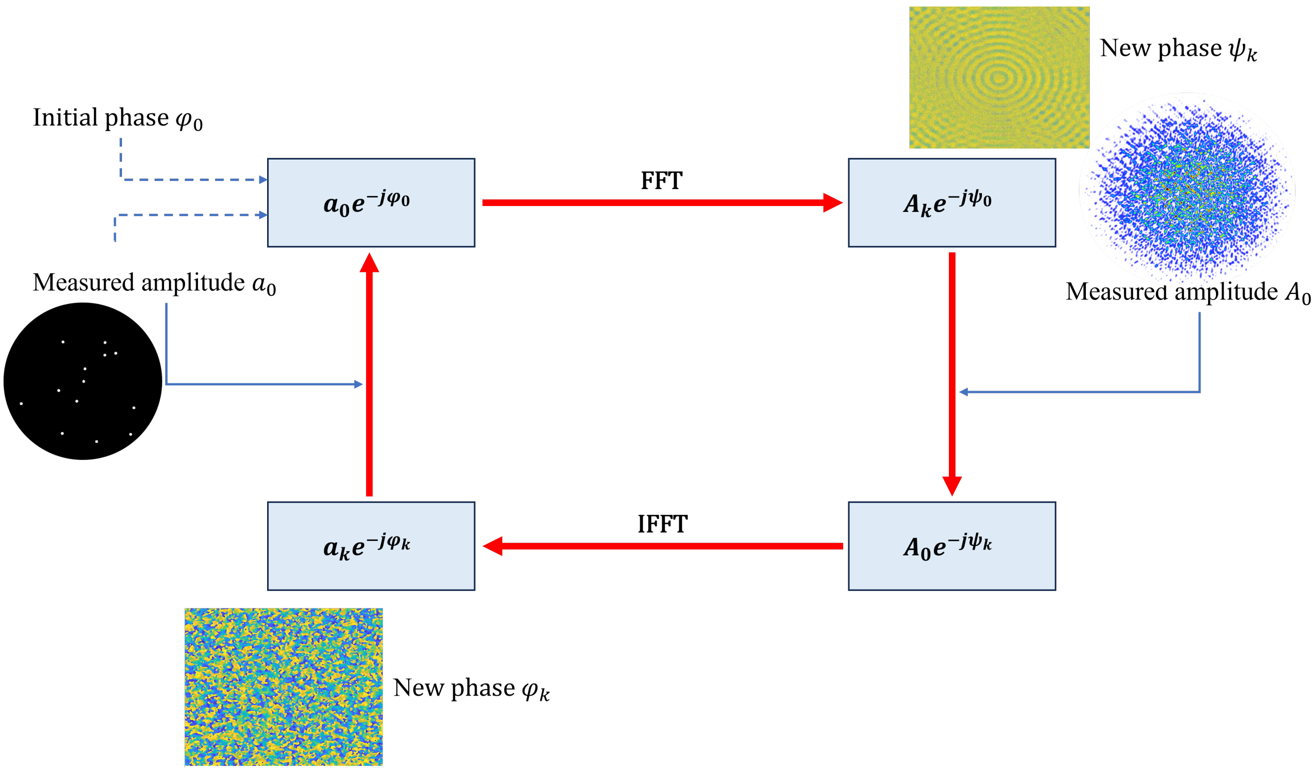

Figure 4.8: Process of one iteration in the program.

The program starts with a zero-phase guess inside the pinholes. It then runs a loop for N iterations. In each loop, the near-field wave is transformed to the far field using an FFT. We keep the calculated far-field phase, but replace the calculated amplitude with the measured amplitude. Next, this updated wave is transformed back to the near field using an inverse FFT. Finally, we apply the digital mask constraint again and keep the phase inside the holes. The mask matrix forces the light outside the holes to zero, and resets the amplitude inside the holes to a uniform value.

After the loop finishes, the final phase can be extracted from each pinhole. To avoid phase wrapping errors, the program will average the phase inside each hole using complex numbers. Instead of averaging the raw phase angles directly which can cause jumps when values fluctuate around the $\pm\pi$ boundary, the pixels within each pinhole region are projected onto the complex plane as unit vectors, averaged, and then converted back to a single angle. Finally, the program will fit these discrete phase values to standard Zernike polynomials using the least-squares method. To achieve this, the centroid coordinates of all pinholes across all rotations are extracted and normalized by the maximum radial position. A design matrix is then constructed, containing the standard Zernike polynomials evaluated at these normalized polar coordinates, along with independent piston terms for each rotation to compensate for any global phase shifts between different measurements. The global Zernike coefficients are finally calculated by solving this overdetermined linear system. This step helps us reconstruct the continuous wavefront and analyze the aberrations.

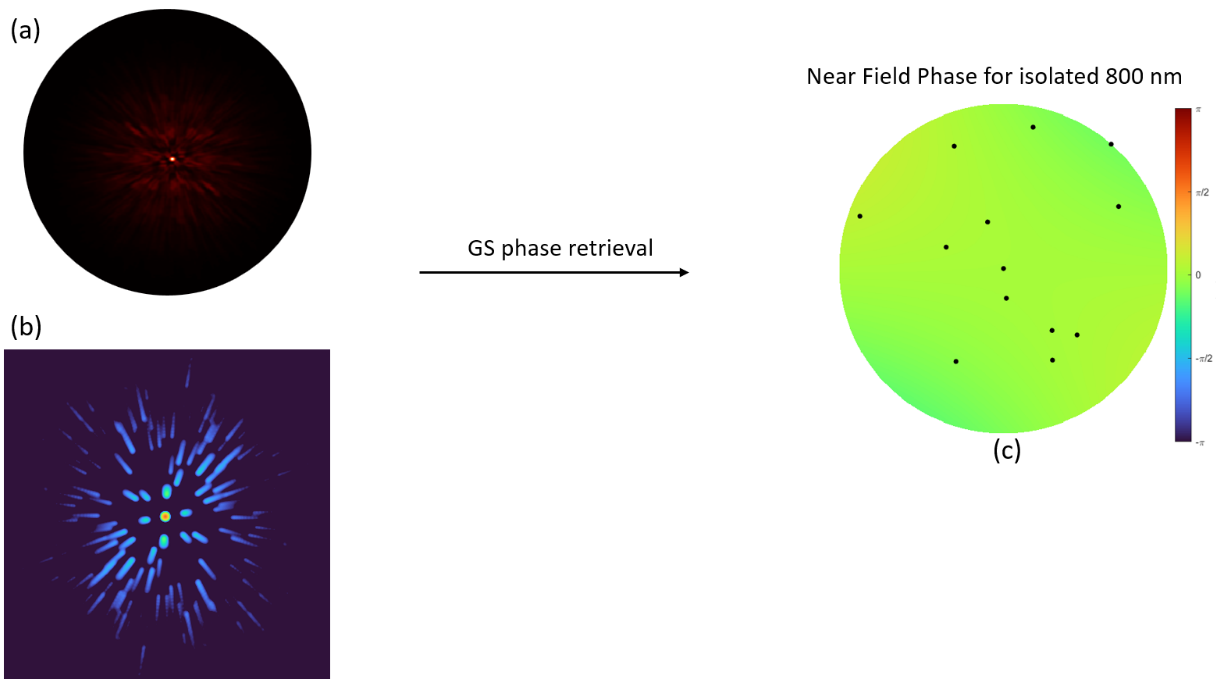

Figure 4.9: An simulated broadband pulse and retrieved near-field phase. (a) Far-field intensity of the simulated broadband pulse; (b) FFT of the far-field intensity; (c) Near-field phase retrieval for isolated 800 nm.

4.4.3 Simulation of broadband pulses

To verify the ability of the digital filter and the GS algorithm in isolating monochromatic far-field intensity and retrieving near-field phase, we simulated the broadband pulses (750 nm to 1000 nm) generated from the multi-terawatt OPCPA laser. The simulated pulses pass through the mask with 12 holes (Mask 1) and are focused by an off-axis parabolic mirror with an apparent focal length of 445 mm, as same as the laboratory conditions. Figure 4.9 shows the result of the simulation.

In the simulation, the monochromatic far-field intensity of 800 nm was isolated by the digital filter. Its near-field phase was retrieved by the GS algorithm, as shown in Figure 4.9 (c). The Zernike coefficients (y-tilt, x-tilt, oblique astigmatism, vertical astigmatism, and defocus) of this simulation are close to zero and the near-field wavefront is almost flat, which agrees with the simulation without any aberrations.

5 Result and Discussion

5.1 Fiber-coupled diode laser

Since the fiber-coupled diode laser was used for the initial test and the development of the wavefront retrieval program, the only IMPALA mask used here is the one with 12 pinholes, i.e. Mask 1. This mask does not require rotation and thus has less data, which can make the early-stage program development easier.

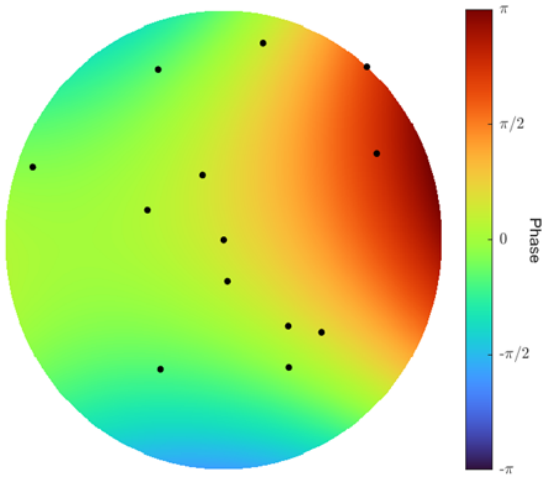

Figure 5.1: Retrieved wavefront of the 523 nm fiber-coupled diode laser. The black dots are the distributions of the pinholes.

As shown in Figure 5.1, the retrieved near-field wavefront of the fiber-coupled diode laser is not flat, which could be reasonable, because aberrations are corrected by manually adjusting the optical elements based on observations of the laser beam profile during the measurement. Thus, these unavoidable aberrations are captured by the phase retrieval program, and the Zernike decomposition of the main aberrations are y-tilt = 0.74 rad, x-tilt = 0.38 rad, astigmatism = 0.26 rad and defocus = −0.095 rad. It shows that the phase retrieval program is capable of reconstructing the near-field wavefront from a monochromatic far-field intensity. This suggests that it can be used to measure the wavefront and aberrations of the multi-terawatt laser system, once the monochromatic intensity can be isolated.

5.2 The multi-terawatt laser system

Two different masks (12 pinholes, Mask 1 and 10 pinholes, Mask 2) were used for the wavefront characterization of the multi-terawatt laser system. In the experiments, the deformable mirror (DM) inside the beamline was used for optimizing the initial wavefront and introduced different aberrations (astigmatism, x-coma and primary spherical) for the measurements to test the accuracy of the IMPALA technique. The parameter a_n in μm is the root-mean-square deformation of the laser wavefront [25]. For different aberrations in the experiments, we introduced $a_2 = 0.1$ for astigmatism, $a_3 = 0.3$ for x-coma and $a_4 = 0.249$ for primary spherical.

According to the spectral resolution calculated before and the spectrum of the multi-terawatt laser, the isolated wavelengths will be 770 nm, 800 nm and 830 nm. Although the central wavelength of the laser should be 850 nm, the camera sensor is more sensitive to light below 850 nm. Thus, the range of the IMPALA streaks is from about 750 nm to 850 nm.

5.2.1 Measurement with Mask 1

To test the single-shot capability of the IMPALA method, we performed an independent measurement using a mask with 12 pinholes. The mask was not rotated during this test. The laser beam was focused and no additional aberrations were introduced. Figure 5.2 shows the recovered spectrally resolved wavefronts and their Zernike coefficients.

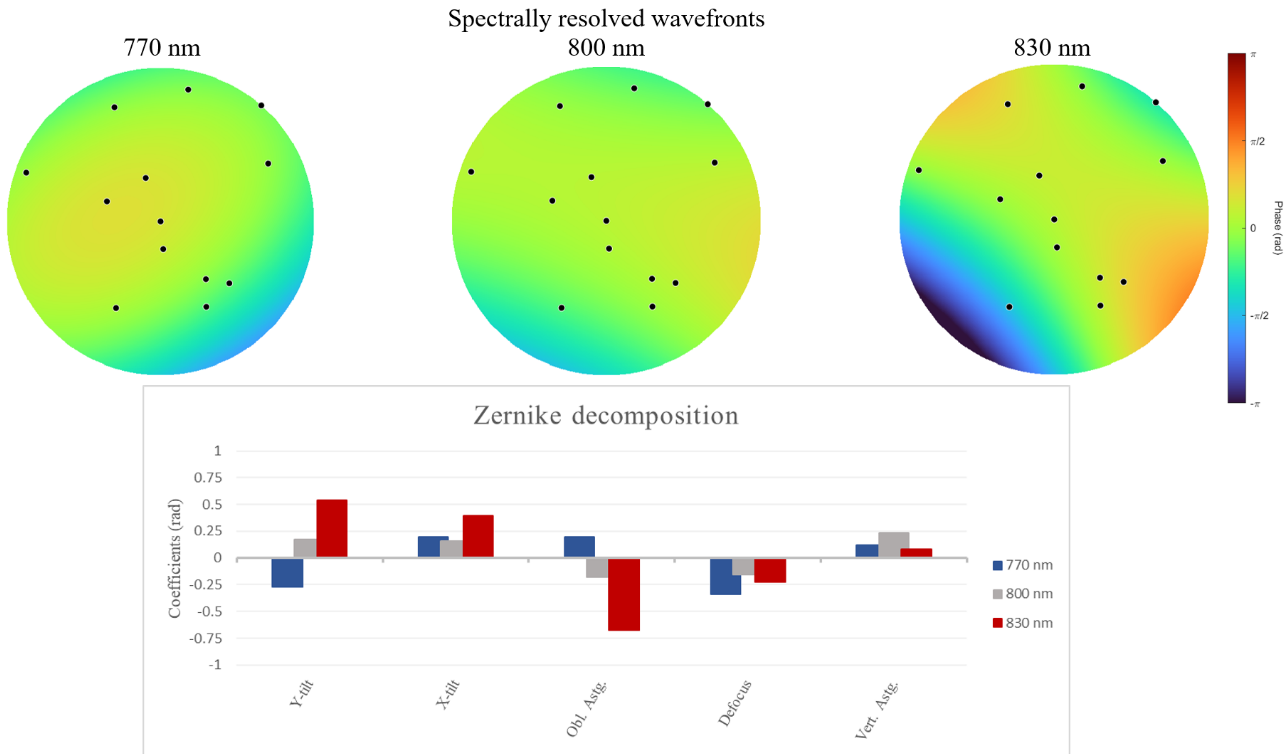

Figure 5.2: Retrieved near-field wavefronts (above) for three different wavelengths (redder: 830 nm; central: 800 nm; bluer: 770 nm)

Because there are only 12 sampling pinholes, the spatial resolution of the reconstructed wavefronts is relatively low compared to the multiple rotation mask that will be discussed later. However, the sampling is still able to capture the main low-order aberrations. Looking at the retrieved wavefront, the 800 nm wavefront is mostly green and uniform. This shows that the wavefront was optimized by the DM, which matches the actual experiment. In contrast, the 830 nm wavefront displays a strong color gradient from blue to orange. This may indicate severe phase distortions at the red edge of the laser spectrum.

The Zernike decomposition chart below Figure 5.2 confirms these visual results. For 800 nm (grey bars), all major coefficients are close to zero. This suggests that the system is well aligned for this wavelength. However, for 830 nm (red bars), the coefficients change dramatically. The y-tilt increases to about 0.55 rad, and the x-tilt reaches about 0.40 rad. As discussed earlier, this chromatic variation can lead to pulse-front tilt (PFT). Additionally, the oblique astigmatism drops to about -0.70 rad at 830 nm.

In conclusion, the 12-hole mask provides a lower spatial resolution because of the limited sampling points. However, the results show its ability to detect the low-order aberrations and spatiotemporal couplings (STCs), such as chromatic tilt and astigmatism. The mask can be an effective and fast tool for single-shot laser diagnostics in real-time experiments.

5.2.2 Measurement with Mask 2

Focus measurement without introduced aberrations

Before measurement, the beam was first optimized by the DM without introducing any aberrations. Noted that the DM has a default defocus parameter $a = -10.74$. The spectrally resolved wavefronts and their Zernike decomposition in Figure 5.3 shows the chromatic evolution across the pulse spectrum. At 800 nm (central) and 770 nm (bluer), the wavefronts are mostly flat (illustrated by the uniform green color), representing a well-optimized phase profile by utilizing DM. The phase maps of these two wavelengths both exhibit a mild gradient from the top-left to the bottom-right, indicating the presence of low-order aberrations, primarily a slight tilt and coma. At 830 nm (redder), the wavefront has more artifacts in the bottom-right, which is a classic pattern of astigmatism coupled with spatial tilt. The results of this measurement can work as a baseline for other measurements with introduced aberrations.

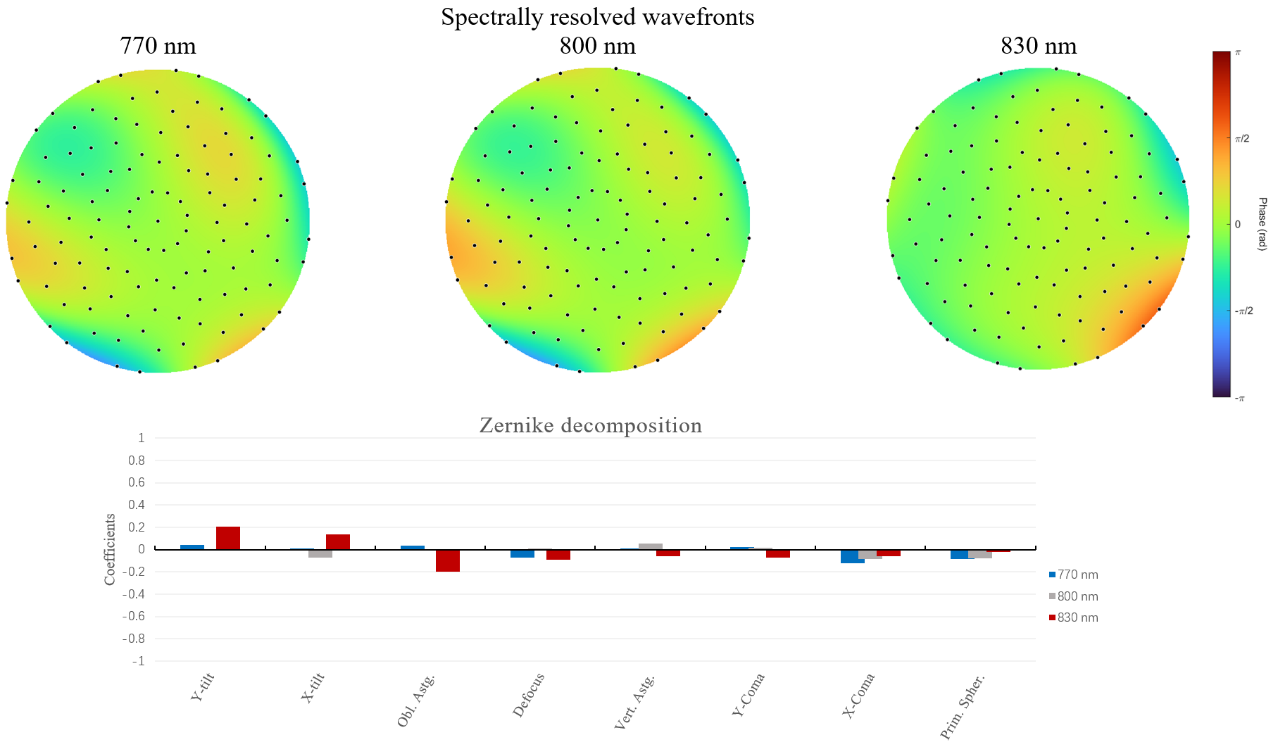

Figure 5.3: Retrieved near-field wavefronts (above) for three different wavelengths (redder: 830 nm; central: 800 nm; bluer: 770 nm) after 12 rotations with Mask 2, and their Zerinike decomposition (below) of the main terms.

Table 5.1: Zernike coefficients of the focus measurement.

	Z_{770nm} (rad)	Z_{800nm} (rad)	Z_{830nm} (rad)
Y-tilt	0.039	-0.006	0.204
X-tilt	0.008	-0.069	0.138
Oblique astigmatism	0.034	-0.011	-0.198
Defocus	-0.069	0.010	-0.093
Vertical astigmatism	0.009	0.053	-0.060
Y-Coma	0.024	0.019	-0.072
X-Coma	-0.122	-0.082	-0.056
Primary spherical	-0.083	-0.078	-0.021

The initial observations can be proven and go a step further by analyzing the extracted Zernike coefficients Z_λ as shown in Table 5.1 and Figure 5.3 below. At 800 nm (grey), all Zernike coefficients (y-tilt, x-tilt, astigmatism, defocus, coma, and primary spherical) are tightly near zero (within ± 0.05 rad). The results confirm that the system is well-aligned by the DM.

There is a chromatic variation in the spatial tilt coefficients (y-tilt and x-tilt). At 770 nm and 800 nm, the tilt values are negligible. At 830 nm, the y-tilt jumps to 0.2 rad and the x-tilt to approximately 0.15 rad. A wavefront tilt that varies linearly or non-linearly with wavelength is defined as spatial chirp. In the spatiotemporal domain, this spatial dispersion manifests as PFT. This indicates that the 830 nm spectral component is propagating at a slightly different angle relative to the rest of the pulse, likely due to residual angular dispersion from the compressors [9].

Another main aberration here is the oblique astigmatism. While it remains near zero for 770 nm and 800 nm, it drops sharply to -0.2 rad at 830 nm. This could originate from off-axis reflections on slightly deformed mirrors.

Introduced vertical astigmatism

The Zernike coefficients from the focus measurement can be a baseline to test the accuracy of the phase retrieval program. The DM introduces the same aberration to all the spectrum components.

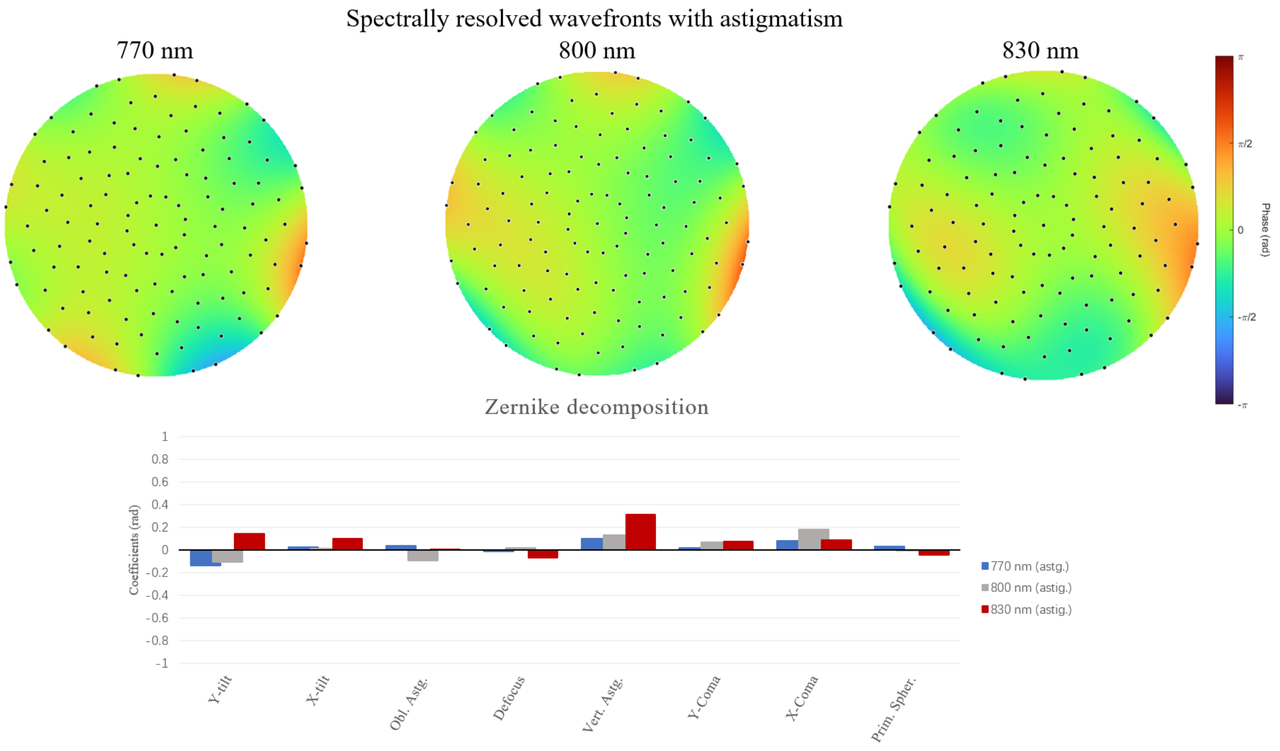

Figure 5.4: Retrieved near-field wavefronts (above) and their Zernike decomposition (below) with introduced vertical astigmatism.

Table 5.2: Zernike coefficients of the vertical astigmatism measurement.

	Z_{770nm} (rad)	Z_{800nm} (rad)	Z_{830nm} (rad)
Y-tilt	-0.139	-0.103	0.142
X-tilt	0.024	0.015	0.101
Oblique astigmatism	0.039	-0.091	0.001
Defocus	0.011	0.017	-0.069
Vertical astigmatism	0.099	0.134	0.315
Y-Coma	0.019	0.067	0.075
X-Coma	-0.080	0.180	0.090
Primary spherical	-0.031	-0.003	-0.040

The new spectrally resolved wavefronts and their Zernike coefficients Z_λ are shown in Figure 5.4 and Table 5.2. Compared to the focus measurement, the wavefronts now display a "saddle" shape, which is a classic pattern for astigmatism. The Zernike decomposition also shows a significant increase in the vertical astigmatism coefficient for 830 nm (red bar).

The accuracy of the algorithm can be verified by comparing the measured results with the theoretical values. The DM introduced an optical path difference of 0.1 μm. Because our Zernike polynomials use RMS normalization, the theoretical change in the vertical astigmatism coefficient (ΔZ) for a specific wavelength (λ) is calculated by:

$$\Delta Z_{expected} = \frac{0.1 \times 2\pi}{\lambda \times \sqrt{6}} \ \mu\text{m} \tag{5.1}$$

At 830 nm ($\lambda = 0.83$ μm), the expected change is $\Delta Z \approx 0.309$ rad. From our table, the measured vertical astigmatism changed from -0.0597 rad to 0.3145 rad. The measured difference is 0.3742 rad. This result matches the theoretical value very well. The small difference (about 20%) is common and usually caused by minor pupil size calibration errors between the DM and the software. At 800 nm ($\lambda = 0.80$ μm), the expected change is $\Delta Z \approx 0.321$ rad. However, the measured difference is only $0.1340 - 0.0527 = 0.0813$ rad. At 770 nm ($\lambda = 0.77$ μm), the expected change is $\Delta Z \approx 0.333$ rad. The measured difference is only $0.0984 - 0.0089 = 0.0895$ rad.

The results show reasonable agreement between the retrieved and expected values of the quantitative phase amplitude at 830 nm. Although for 800 nm and 770 nm, the measured changes are smaller than expected, they both have the same level of increased vertical aberrations.

Introduced primary spherical

To further investigate the ability of this phase retrieval method, a large, high-order aberration: 0.249 μm of primary spherical aberration was introduced by the DM . The retrieval of the wavefront was analyzed at the 800 nm, which can offer a better isolated image quality.

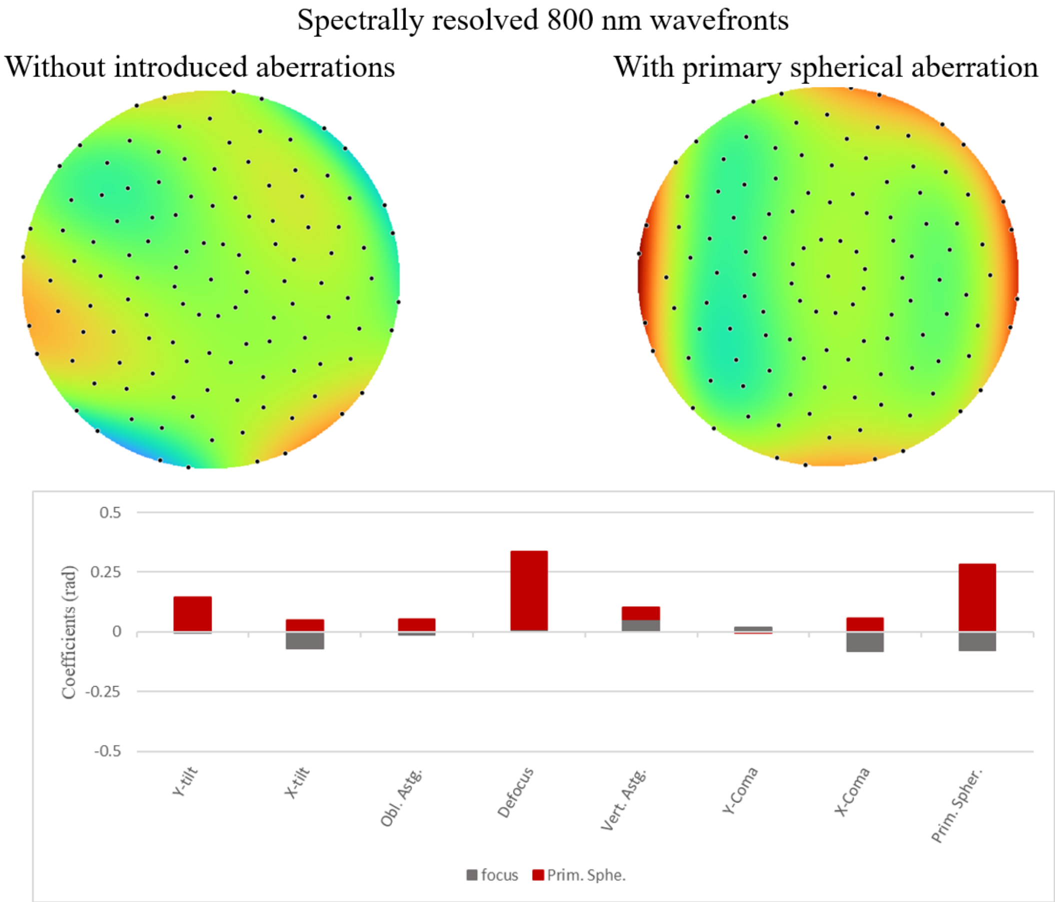

Figure 5.5: (Left) Retrieved isolated 800 nm wavefront without introduced aberrations; (Right) Retrieved isolated 800 nm wavefront with spherical aberration; (Below) Zernike decomposition of two wavefronts. Red bars correspond to primary spherical aberration, and grey bars correspond to data at focal spot without aberrations.

The spectrally resolved wavefronts and their Zernike coefficients are shown in Figure 5.5. Without the introduced aberration, the 800 nm wavefront is flat and uniform, as discussed above. After introducing the aberration, the wavefront displays a symmetric circular pattern with red edges. This can be the shape of primary spherical aberration. The Zernike decomposition (Figure 5.5 below) also confirms a large increase in the primary spherical coefficient (red bar). Additionally, the defocus coefficient term increases significantly. This is expected, as the DM introduces defocus to balance the overall phase error when generating a large spherical aberration.

Retrieving this large and high-order aberration was challenging. The standard GS algorithm with a flat initial phase failed to reconstruct the wavefront, as it easily became trapped in local minimum. To solve this, we implemented a modified GS algorithm. For each rotation, multiple random initial phases will be generated and run a fast loop of 300 iterations. We selected the initial phase with the lowest error as the best starting point. Then, the Hybrid Input-Output (HIO) method is used to recover the final phase. The expected change for the primary spherical coefficient

(ΔZ) at 800 nm is calculated by:

$$\Delta Z_{expected} = \frac{0.249 \times 2\pi}{\lambda \times \sqrt{5}} \approx 0.875 \text{ rad} \tag{5.2}$$

From the phase retrieval method, the coefficient changed from -0.08 rad (focus) to 0.28 rad (with aberration), making a measured difference of 0.36 rad.

Although the modified GS algorithm successfully recovered the shape of the spherical aberration, the measured amplitude (0.36 rad) is lower than the expected value (0.875 rad). This result shows the limitation of the IMPALA method. A large spherical aberration creates high spatial frequencies, which cause the signal to spread out widely in the Fourier plane. To capture these high frequencies, we had to increase the size of our spatial filter window. However, a larger window approaches the spectral resolution limit of the IMPALA mask. It inevitably mixes the signals from neighboring wavelengths (such as 790 nm or 810 nm). This mixing disturbs the isolated far-field intensity. As a result, even the algorithm will miscalculate the final phase amplitude. Also, the DM could not fully introduce this high-order aberration, and thus the expected change for the Zernike coefficient could be lower than 0.875 rad. This indicates that the current mask design is more effective for low-order STCs, but the spherical aberration case shows that the current implementation still has limitations for larger high-order aberrations. Adjustments (such as smaller pinholes to give a better resolution) are needed to measure large, high-order aberrations.

Spectral bandwidth of IMPALA

Because of the quantum efficiency of the Sony IMX178 camera sensor as shown in Figure 5.6, the spectral bandwidth of IMPALA in this is not as broad as expected (from 750 nm to 1000 nm). The camera has a higher sensitivity below 850 nm. To avoid saturating the camera, the intensity of lights above 850 will be hard to record.

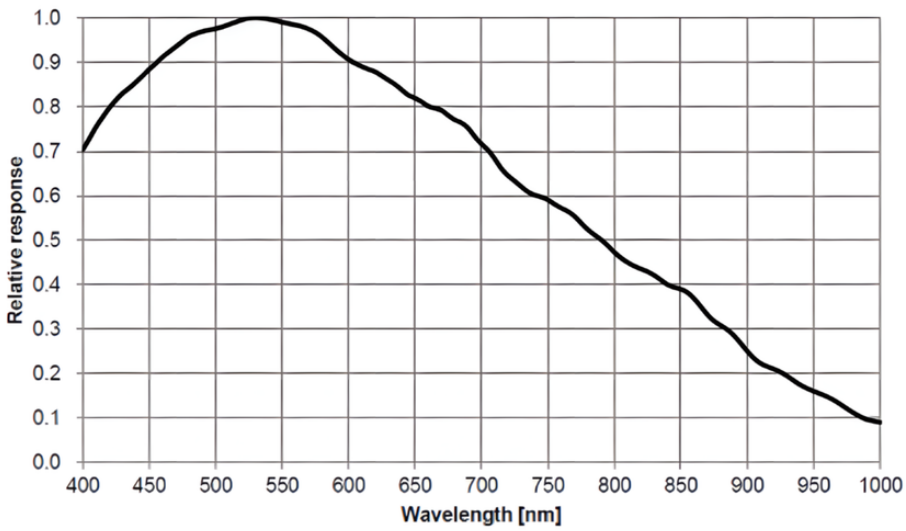

Figure 5.6: Relative quantum efficiency of Sony IMX178 [26]

As described in Chapter 4, the theoretical position of different wavelengths in the Fourier plane can be calculated by Equation 4.7. As shown in Figure 5.7, the simulated monochromatic speckles centered at 750 nm and 850 nm reach the edges of the streaks from the Fourier transform of the far-field intensity. This shows that the spectral range that can be isolated is from 750 nm to 850. Otherwise the filter window will be out of the streaks in the Fourier plane, resulting in blurred monochromatic intensity.

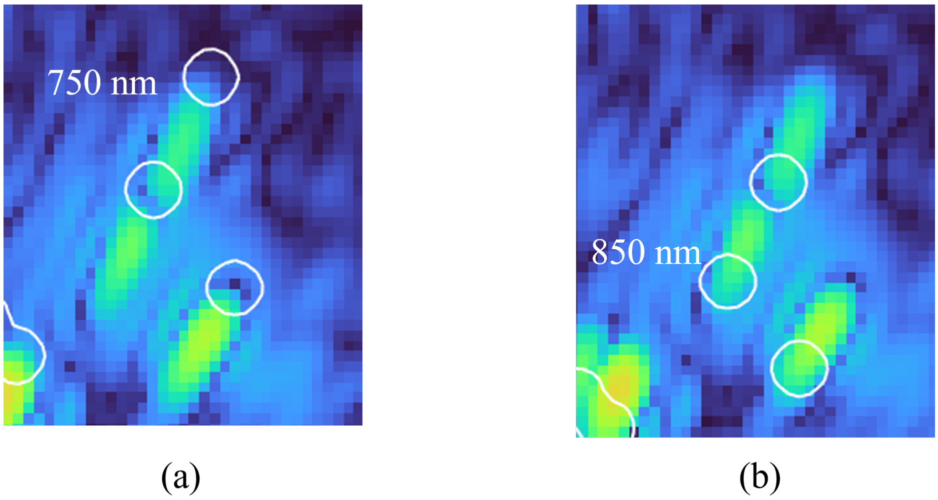

Figure 5.7: Simulated position for monochromatic speckles centered at different wavelengths in Fourier plane.

6 Conclusion and outlook

In this project, the IMPALA technique was successfully implemented and optimized to characterize the spatiotemporal couplings (STCs) of a multi-terawatt OPCPA laser system. The method was first validated on a continuous-wave fiber laser and then applied to the broadband high-power laser system. This chapter will give a brief summary and outlook for future work.

6.1 Summary of results

The measurements, using both a single-shot mask with 12 holes and a multi-rotation mask with 10 holes, showed its ability to reveal STCs in the OPCPA system. The tests with introduced astigmatism and primary spherical aberration in Chapter 5 showed that the introduced aberrations can be captured by IMPALA and quantified using Zernike decomposition. For low-order aberrations, the system is able to retrieve a 0.1 μm astigmatism at 830 nm, while the measured differences for 770 nm and 800 nm are smaller than the expected values. For high-order aberrations, this method is not able to accurately retrieve the corresponding values, while it is able to detect the difference in the primary spherical and defocus terms. This could be the limitation caused by its process during isolating the far-field intensity in the Fourier plane. When processing the data with high-order aberrations, the window size of the filter becomes more important. A small window will miss the surrounding signals, while a large window might cause the mixing from neighboring wavelengths. A better spectral resolution may solve this problem, which can be improve by using smaller pinholes, i.e. smaller beamlets' diameter. The beamlets' diameter in this project is 0.8 mm, while the one in [9] is 0.15 mm, giving a spectral resolution of approximately 10 nm.

Standard Gerchberg-Saxton (GS) algorithms used in this technique will be trapped in local minimum. Thus, more advanced phase-retrieval algorithms are necessary. In this project, the Hybrid Input-Output (HIO) algorithm was also tested. This advanced algorithm recovered the complex spherical wavefront pattern.

6.2 Outlook

Future work should focus on overcoming these hardware and algorithmic limitations to fully retrieve the phase and characterize STCs in ultra-short laser pulses.

First, the design of the mask can be improved. To accurately measure large and high-order aberrations without spectral overlapping, we need to increase the separation distance between the beamlets in the spatial-frequency domain. This can be achieved by designing a mask with a larger pinhole spacing or using focusing optics with a longer focal length. The current camera restricts the spectral dynamic range of IMPALA to wavelengths below 850 nm, missing the actual central wavelength and longer infrared wavelengths of the OPCPA system. In future work, enhancing the spectral bandwidth is possible by applying bandpass filters [27].

The phase retrieval algorithm architecture can be further improved. Currently, the multi-rotation measurements reconstruct the phase for 10 holes at a time. The 120 total sampled points are only combined during the final Zernike fitting. This independent, divided processing can lead to phase inconsistencies. A global GS algorithm should be developed to evaluate all 120 points simultaneously during the iterations. This would provide a stronger constraint, preventing mode aliasing and ensuring a continuous wavefront.

Bibliography

[1] "Compression of amplified chirped optical pulses". In: *Opt. Commun.* 56.3 (1985), pp. 219–221. ISSN: 0030-4018. DOI: 10.1016/0030-4018(85)90120-8.

[2] Spencer W Jolly, Olivier Gobert and Fabien Quéré. "Spatio-temporal characterization of ultrashort laser beams: a tutorial". In: *J. Opt.* 22.10 (2020), p. 103501. DOI: 10.1088/2040-8986/abad08.

[3] Hampus Wikmark, Chen Guo, Jan Vogelsang, Peter W. Smorenburg, Hélène Coudert-Alteirac, Jan Lahl, Jasper Peschel, Piotr Rudawski, Hugo Dacasa, Stefanos Carlström, Sylvain Maclot, Mette B. Gaarde, Per Johnsson, Cord L. Arnold and Anne L'Huillier. "Spatiotemporal coupling of attosecond pulses". In: *Proc. Natl. Acad. Sci. U.S.A.* 116.11 (2019), pp. 4779–4787. DOI: 10.1073/pnas.1817626116. eprint: https://www.pnas.org/doi/pdf/10.1073/pnas.1817626116.

[4] Erik Löfquist, Cornelia Gustafsson, Andrea Angella, Anders Persson and Olle Lundh. "Correlated x-ray and electron beam steering by pulse-front tilt in laser wakefield acceleration". In: *Phys. Rev. Accel. Beams* 28 (10 2025), p. 102802. DOI: 10.1103/cq83-8kfb.

[5] C. Iaconis and I. A. Walmsley. "Spectral phase interferometry for direct electric-field reconstruction of ultrashort optical pulses". In: *Opt. Lett.* 23.10 (1998), pp. 792–794. DOI: 10.1364/OL.23.000792.

[6] V. Gallet, S. Kahaly, O. Gobert and F. Quéré. "Dual spectral-band interferometry for spatio-temporal characterization of high-power femtosecond lasers". In: *Opt. Lett.* 39.16 (2014), pp. 4687–4690. DOI: 10.1364/OL.39.004687.

[7] Gustave Pariente, Valentin Gallet, A. Borot, Olivier Gobert and Fabien Quere. "Space–time characterization of ultra-intense femtosecond laser beams". In: *Nat. Photonics* 10 (July 2016). DOI: 10.1038/nphoton.2016.140.

[8] Antonin Borot and Fabien Quéré. "Spatio-spectral metrology at focus of ultrashort lasers: a phase-retrieval approach". In: *Opt. Express* 26.20 (2018), pp. 26444–26461. DOI: 10.1364/OE.26.026444.

[9] Slava Smartsev, Aaron Liberman, Igor A. Andriyash, Antoine Cavagna, Alessandro Flacco, Camilla Giaccaglia, Jaismeen Kaur, Joséphine Monzac, Sheroy Tata, Aline Vernier, Victor Malka, Rodrigo Lopez-Martens and Jérôme Faure. "Simple few-shot method for spectrally resolving the wavefront of an ultrashort laser pulse". In: *Opt. Lett.* 49.8 (2024), pp. 1900–1903. DOI: 10.1364/OL.502000.

[10] Slava Smartsev, Sheroy Tata, Aaron Liberman, Michael Adelberg, Arujash Mohanty, Eitan Y Levine, Omri Seemann, Yang Wan, Eyal Kroupp, Ronan Lahaye, Cédric Thaury and Victor Malka. "Characterization of spatiotemporal couplings with far-field beamlet cross-correlation". In: *J. Opt.* 24.11 (2022), p. 115503. DOI: 10.1088/2040-8986/ac9631.

[11] Bahaa EA Saleh and Malvin Carl Teich. *Fundamentals of Photonics*. 3rd. John Wiley & Sons, 2019.

[12] Joseph W Goodman. *Introduction to Fourier Optics*. W. H. Freeman, 2017.

[13] MeetOptics. *Optical Aberrations*. `https://www.meetoptics.com/academy/optical-aberrations`. Accessed: 2026-06-10. 2026.

[14] Gary Smith. *Zernike Polynomials*. University of Arizona, College of Optical Sciences. Accessed: 2026-06-10. 2026. URL: `https://webs.optics.arizona.edu/gsmith/Zernike.html`.

[15] Ralph W Gerchberg and William O Saxton. "A practical algorithm for the determination of phase from image and diffraction plane pictures". In: *Optik* 35.2 (1972), pp. 237–246.

[16] J. H. Seldin and J. R. Fienup. "Numerical investigation of the uniqueness of phase retrieval". In: *J. Opt. Soc. Am. A* 7.3 (1990), pp. 412–427. DOI: `10.1364/JOSAA.7.000412`.

[17] James R Fienup. "Phase retrieval algorithms: a comparison". In: *Appl. Opt.* 21.15 (1982), pp. 2758–2769.

[18] J. R. Fienup and C. C. Wackerman. "Phase-retrieval stagnation problems and solutions". In: *J. Opt. Soc. Am. A* 3.11 (1986), pp. 1897–1907. DOI: `10.1364/JOSAA.3.001897`.

[19] Francisco Javier Salgado-Remacha. "Reducing the variability in random-phase initialized Gerchberg-Saxton Algorithm". In: *Opt. Laser Technol.* 85 (2016), pp. 30–34. ISSN: 0030-3992. DOI: `10.1016/j.optlastec.2016.05.021`.

[20] Changliang Guo, Shi Liu and John T. Sheridan. "Iterative phase retrieval algorithms. I: optimization". In: *Appl. Opt.* 54.15 (2015), pp. 4698–4708. DOI: `10.1364/AO.54.004698`.

[21] Tieyu Zhao and Yingying Chi. "Modified Gerchberg–Saxton (G-S) Algorithm and Its Application". In: *Entropy* 22.12 (2020). ISSN: 1099-4300. DOI: `10.3390/e22121354`.

[22] D L Misell. "A method for the solution of the phase problem in electron microscopy". In: *J. Phys. D: Appl. Phys.* 6.1 (1973), p. L6. DOI: `10.1088/0022-3727/6/1/102`.

[23] Larry A. Coldren, Scott W. Corzine and Milan L. Mashanovitch. *Diode Lasers and Photonic Integrated Circuits*. 2nd. John Wiley & Sons, 2012. ISBN: 978-0-470-48413-5.

[24] Erik Löfquist. "Fundamental and Applied Studies of Laser Plasma Accelerators". PhD Thesis. Lund University, 2026.

[25] Peter Blum, Anna Puchert, Emily Archer, Sören Jalas, Spencer W. Jolly, Jens Osterhoff, Wim P. Leemans, Manuel Kirchen, Andreas R. Maier and Rob J. Shalloo. "Programmable focal elongation and shaping of high-intensity laser pulses using adaptive optics". In: *Opt. Lett.* 51.1 (2026), pp. 9–12. DOI: `10.1364/OL.579664`.

[26] Shuyang Chen, Min Huang, Wenbin Ge, Guangming Wang, Xiangning Lu, Yixin Zhao, Jinlin Chen, Lulu Qian and Zhanchao Wang. “Reconfigurable Multispectral Imaging System Design and Implementation with FPGA Control”. In: *Appl. Sci.* 15 (Dec. 2025), p. 12951. DOI: 10.3390/app152412951.

[27] Cristian Alexe, Aaron Liberman, Saga Westerberg, Andrea Angella, Anda-Maria Talposi, Erik Löfquist, Alice Dumitru, Andrew H. Okukura, Flanish D'Souza, Cornelia Gustafsson, Anders Persson, Chen Guo, Cord Arnold, Olle Lundh, Victor Malka and Daniel Ursescu. *Enhanced dynamic range spatio-spectral metrology of few-cycle laser pulses*. 2026. arXiv: 2603.27815 [physics.optics].

A Appendix

Both of the IMPALA masks are designed and manufactured by the Weizmann Institute of Science. The drawings are shown in Figure A.1.

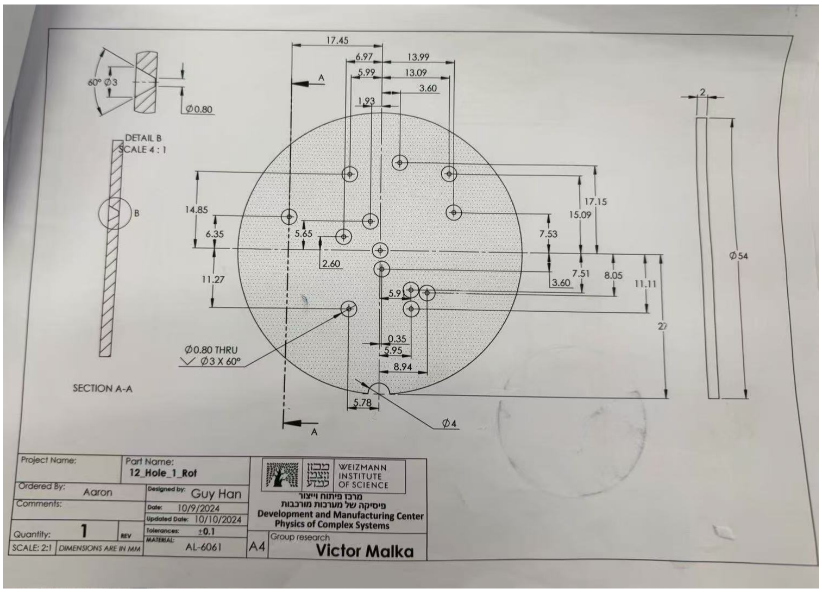

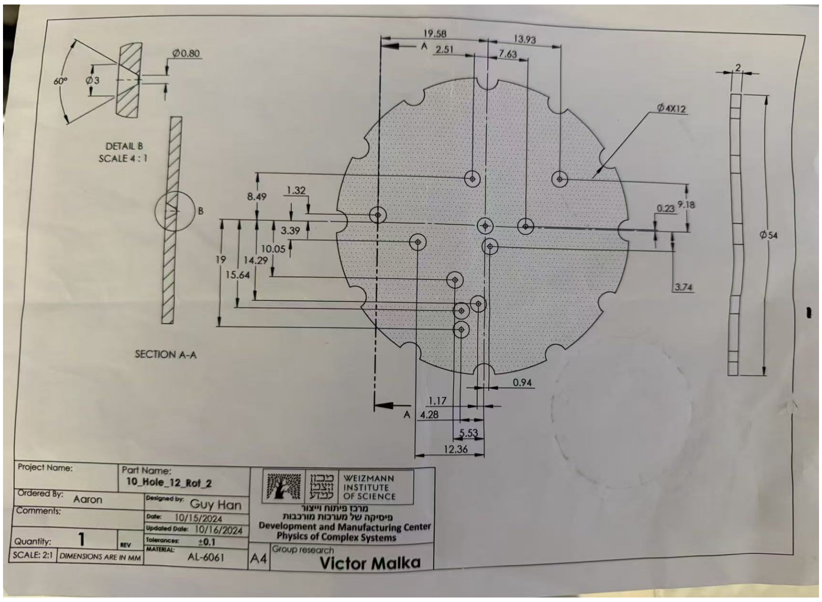

Figure A.1: Design and manufacturing drawings of the masks, produced by Weizmann Institute of Science.

The digital filter was used to isolate monochromatic intensity at 800 nm. The implementation of the digital filter and the recovered far-field intensity are both shown in

Figure A.2. The recovered intensities will serve as the far-field constraint of the GS retrieval program.

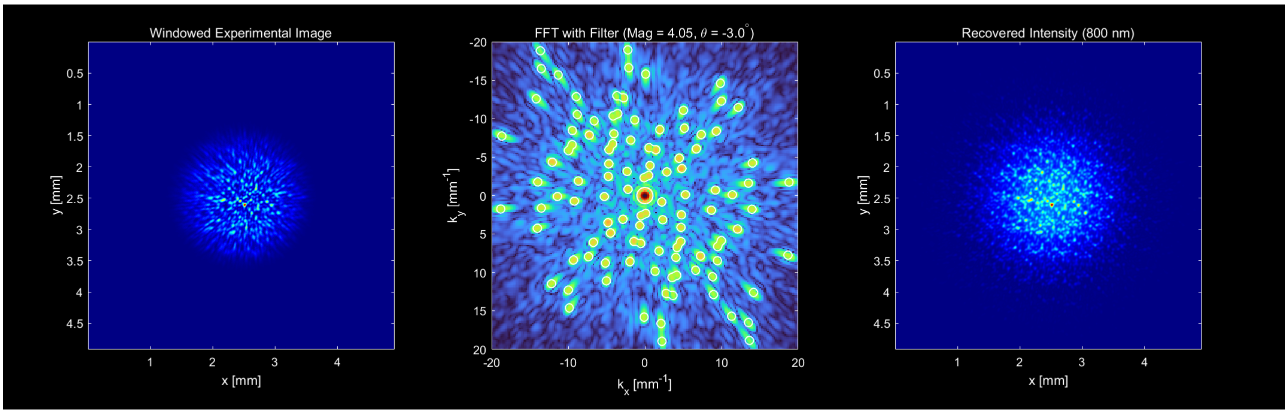

Figure A.2: Calibration of the filter program for far-field intensity measured without additional aberrations. The recovered monochromatic intensity in this case was at 800 nm.